Laminar Cortical Dynamics of 3D Surface Perception: Stratification, Transparency, and Neon Color Spreading

Stephen Grossberg and Arash Yazdanbakhsh[1]

Department of Cognitive and Neural Systems
and
Center for Adaptive Systems
Boston University
677 Beacon Street, Boston, MA 02215
Phone: 617-353-7858
Fax: 617-353-7755
Submitted: January, 2004
Vision Research, in press

All correspondence should be addressed to
Professor Stephen Grossberg
Department of Cognitive and Neural Systems
Boston University
677 Beacon Street
Boston, MA 02215
Phone: 617-353-7858
Fax: 617-353-7755
Email:steve@bu.edu

[1] Authorship in alphabetical order. SG was supported in part by the Air Force Office of Scientific Research (AFOSR F49620-01-1-0397), the National Science Foundation (NSF SBE-0354378) and the office of Naval Research (ONR N00014-01-1-0624). AY was Supported in part by the Office of Naval Research (ONR N00014-01-1-0624)

Abstract

The 3D LAMINART neural model is developed to explain how the visual cortex gives rise to 3D percepts of stratification, transparency, and neon color spreading in response to 2D pictures and 3D scenes. Such percepts are sensitive to whether contiguous image regions have the same contrast polarity and ocularity. The model predicts how like-polarity competition at V1 simple cells in layer 4 may cause these percepts when it interacts with other boundary and surface processes in V1, V2, and V4. The model also explains how: the Metelli Rules cause transparent percepts, bistable transparency percepts arise, and attention influences transparency reversal.

Key Words: Surface Perception, Perceptual Grouping, 3D Figure-Ground Separation, Transparency, Neon Color Spreading

1. Introduction

1.1 Depthful grouping of 2D cues. Refinement of the 3D LAMINART model (Figure 1) enables it to simulate percept of transparency (Figure 2) and neon color spreading (Figures 3). These percepts can be influenced by changing how 2D information is combined from both eyes and by changing the contrast relationships in a 2D picture without changing the geometrical layout of its edges. Such variations provide important clues to how the brain carries out normal 3D vision. Sections 2 and 3 summarize challenging data about these percepts. They are then explained and simulated as emergent properties of all model stages interacting together. Previous versions of the model have clarified how cortical areas V1, V2, and V4 work together to generate other percepts (Grossberg, 1999, 2003; Grossberg and Howe, 2003; Grossberg and Raizada, 2000; Grossberg and Seitz 2003; Grossberg and Swaminathan (2004); Grossberg and Williamson, 2001; Raizada and Grossberg, 2003). The model refinement is needed to extend the model's predictive range to explain the targeted data. This refinement predicts that inhibitory interneurons within layer 4 of V1 prefer to contact cells that are sensitive to the same contrast polarity. This affinity can be explained by models of cortical development (Grossberg and Williamson, 2001), but its implications for perception were previously unclear. The results have been briefly reported in Grosssberg and Yazdanbakhsh (2003a, 2003b).

1.2 Contrast relationships that induce transparency. Many researchers have noted how contrast relations within an image can cause or eliminate a percept of transparency (Adelson, 2000; Anderson, 1997; Beck, 1984; Metelli, 1974; Watanabe and Cavanagh, 1992, 1993). The images in Figure 2 all have the same edge geometry (Figure 2d); however, we perceive them differently. The contrast relations at the figures' X-junction determine the percept. In Figure 2a, the bottom square is perceived as a transparent layer over the top square. The opposite percept, with the bottom square being over the top one, does not occur. Here contrast polarity (dark-light versus light-dark) is preserved along the vertical branch of the X-junction. Moreover, this X-junction branch is part of a surface that is partially occluded by the transparent layer that is attached to the polarity-reversing edge. In Figure 2b, either square can be seen as a transparent surface over the other one. Here contrast polarity is preserved along both X-junction branches, and the percept is bistable. Figure 2c does not induce a percept of transparency. Here polarity-reversal takes place along both branches. Depth stratification does not occur. Instead, the image looks like a bright small square in the middle that is surrounded by two dark L-shaped figures.

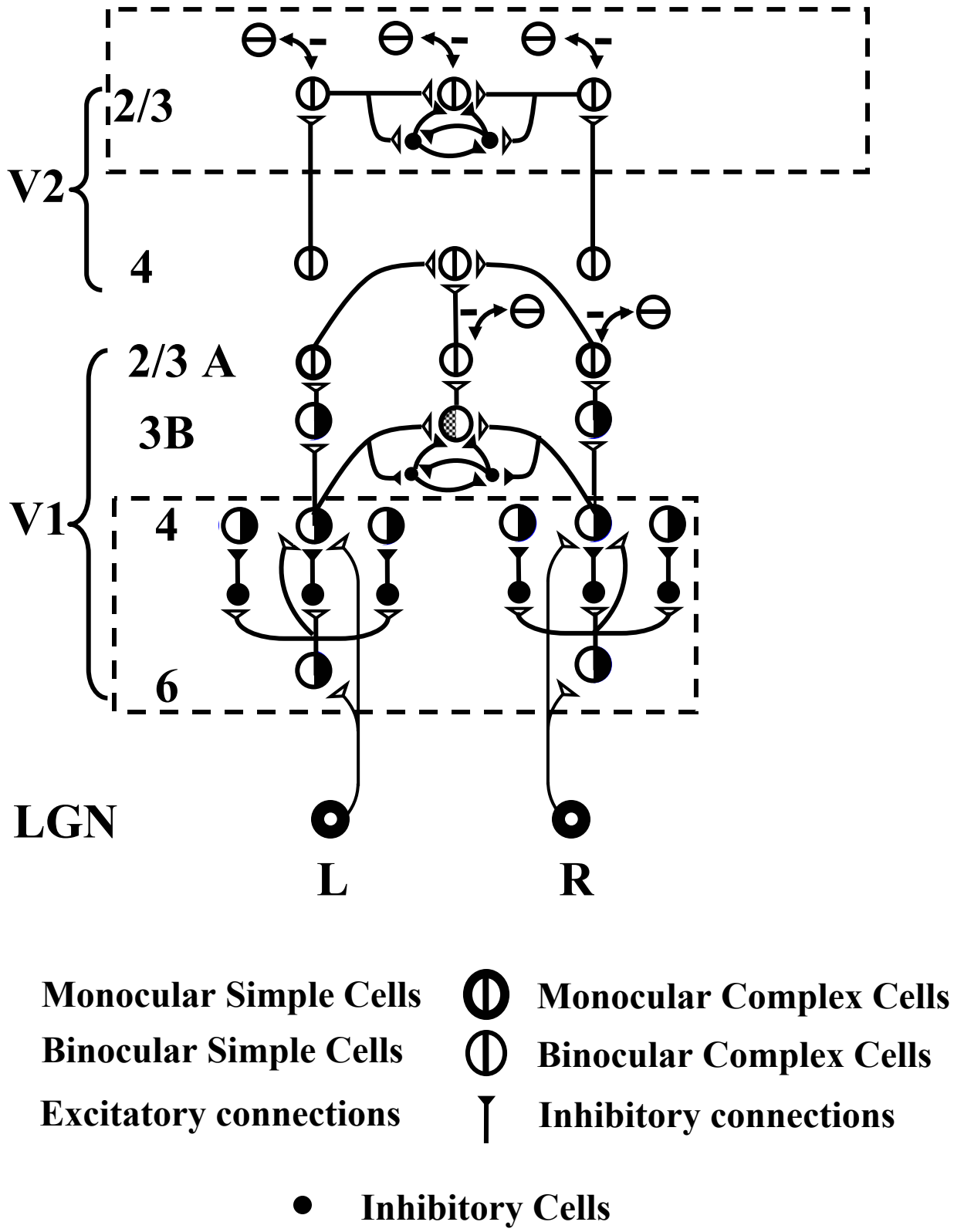

Figure 1. 3D LAMINART model: Before layer 3B of V1, the cells and their connections are eye specific. Like-polarity spatial competition in layer 4 implements the monocular contrast process. Long-range boundary grouping in layer 2/3 of V2 is both binocular and contrast invariant, because opposite eye streams have already been pooled in layer 3B of V1 and layer 4 of V2, and opposite contrasts have already been pooled in layer 2/3 of V1. These laminar circuits clarify how both contrast-polarity sensitive and contrast-polarity pooling processes can coexist together. In the upper dashed box of the figure, a set of vertically-oriented bipole cells are shown, each of them belongs to a group of colinear vertically-oriented bipole grouping cells.

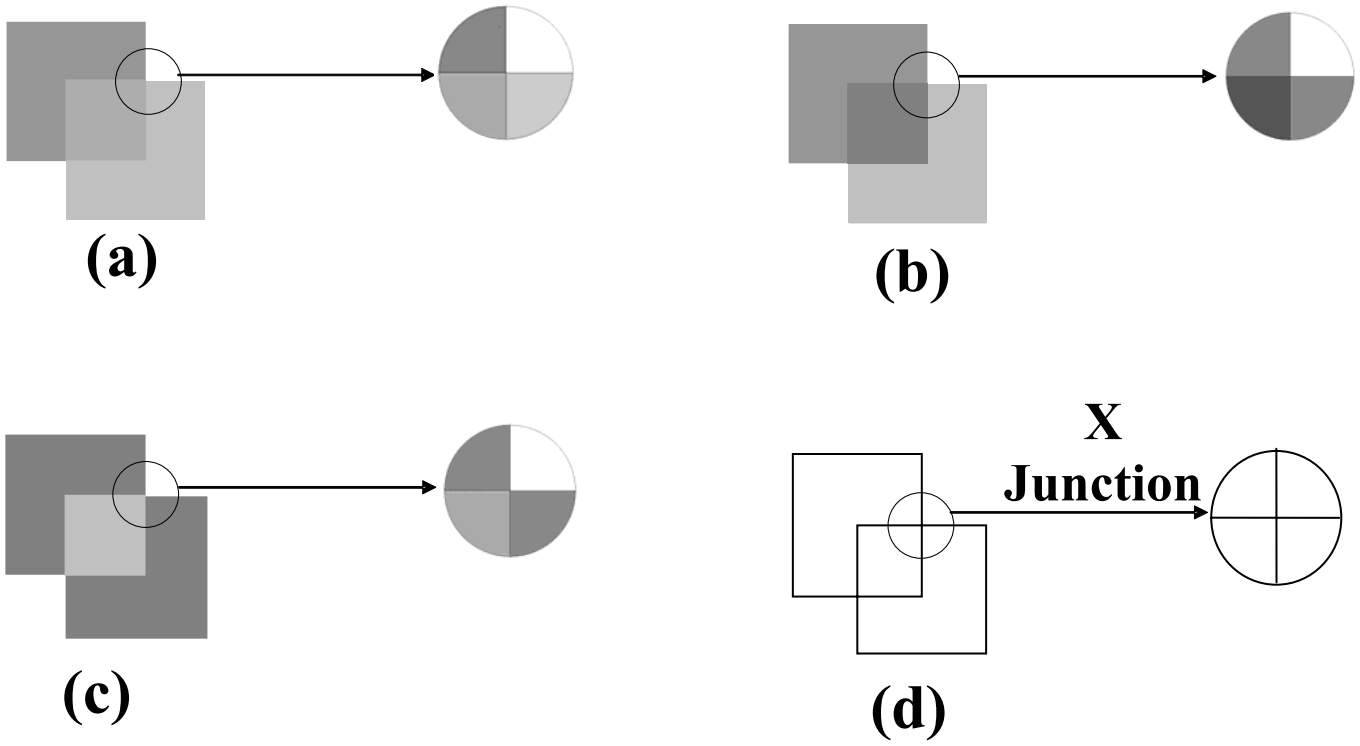

Figure 2. The correspondence between polarity alignment and the presence or absence of transparency: Each panel shows the specific contrast relationship that favors or does not favor transparency. (a) Single polarity reversal favors unique transparency. (b) No polarity reversal favors bistable transparency. (c) Double polarity reversal does not support transparency. (d) All of these images have the same geometry of edges.

These displays show that the relative contrasts at aligned edges of contiguous regions influence whether a transparency percept is perceived. The same contrast polarity at aligned edges of contiguous regions facilitates transparency, whereas opposite contrast polarities prevent transparency. Sensitivity to contrast polarity suggests an influence from an early stage of cortical processing, notably V1. We are therefore led to ask: How does polarity-sensitive V1 processing alter the 3D perceptual groupings that occur in V2, and thus the visible 3D surface percepts that occur in V4?

1.3 Contrast relationships that induce neon color spreading. The different panels of Figure 3 also have the same edge geometry but different contrast relationships again induce different percepts. Neon color spreading occurs when the contrast polarity along the T-junctions is preserved (Figure 3a). Neon is abolished when the polarity along the T-junctions reverses (Figure 3b). The influence of like-polarity contrast relations in neon color spreading also implicates early stages of V1 cortical processing.

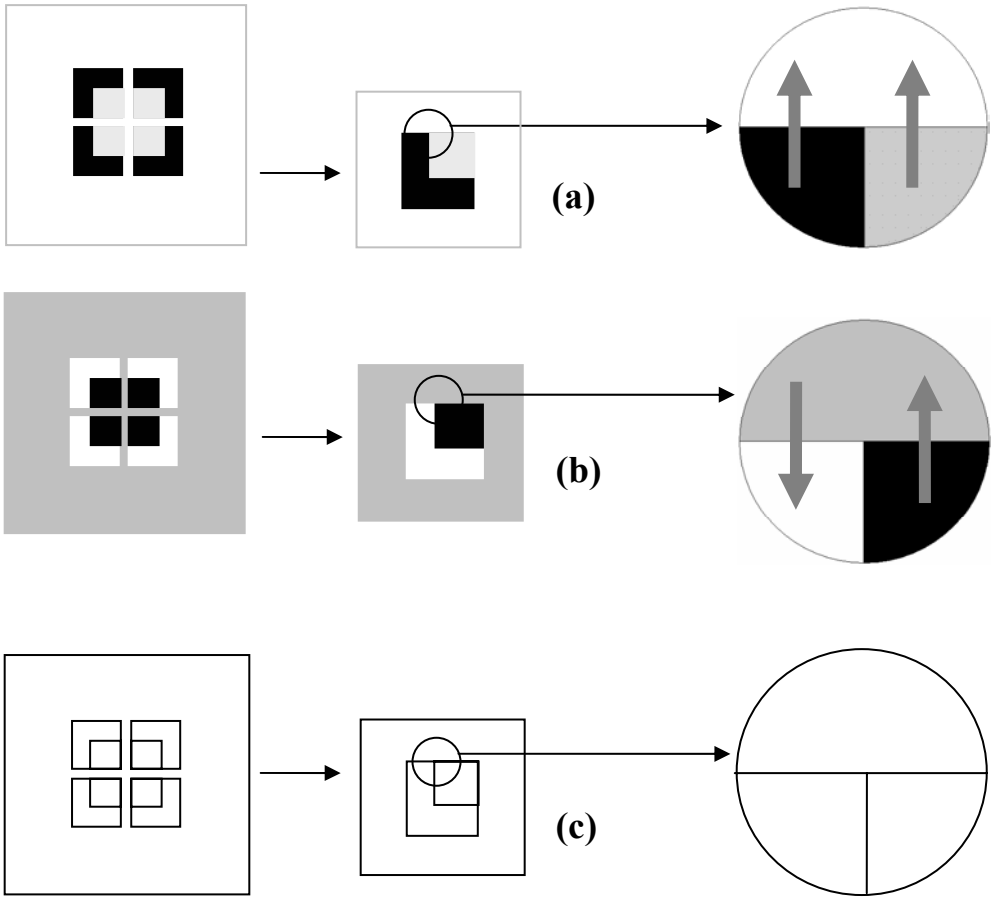

Figure 3. (a) Like-polarity contrasts favor neon color spreading: the T-junction is polarity preserving. (b) Opposite contrast polarities block neon color spreading: the T-junction is polarity reversing. (c) In both (a) and (b), the edge geometry, including all T-junctions, is the same.

1.4 Ocularity of contrast relations in neon color spreading. Takeichi, Shimojo and Watanabe (1993) showed that the contrast polarity constraint that determines neon color spreading is monocular (Figure 4). Fusing the stereogram in Figure 4a, results in a percept of neon color spreading bounded by an illusory square. However, fusing the stereogram in Figure 4b does not result in neon color spreading. The contrast relation that favors neon spreading thus needs to be present completely in one eye. We localize this constraint to layer 4 of cortical area V1, as indicated below.

1.5 Contrast-polarity sensitivity versus contrast-polarity pooling. Another constraint on contrast polarity further localizes the monocular contrast constraint, but seems at the outset to be at odds with it. Figure 5 illustrates that perceptual boundaries can form around objects in front of textured backgrounds.

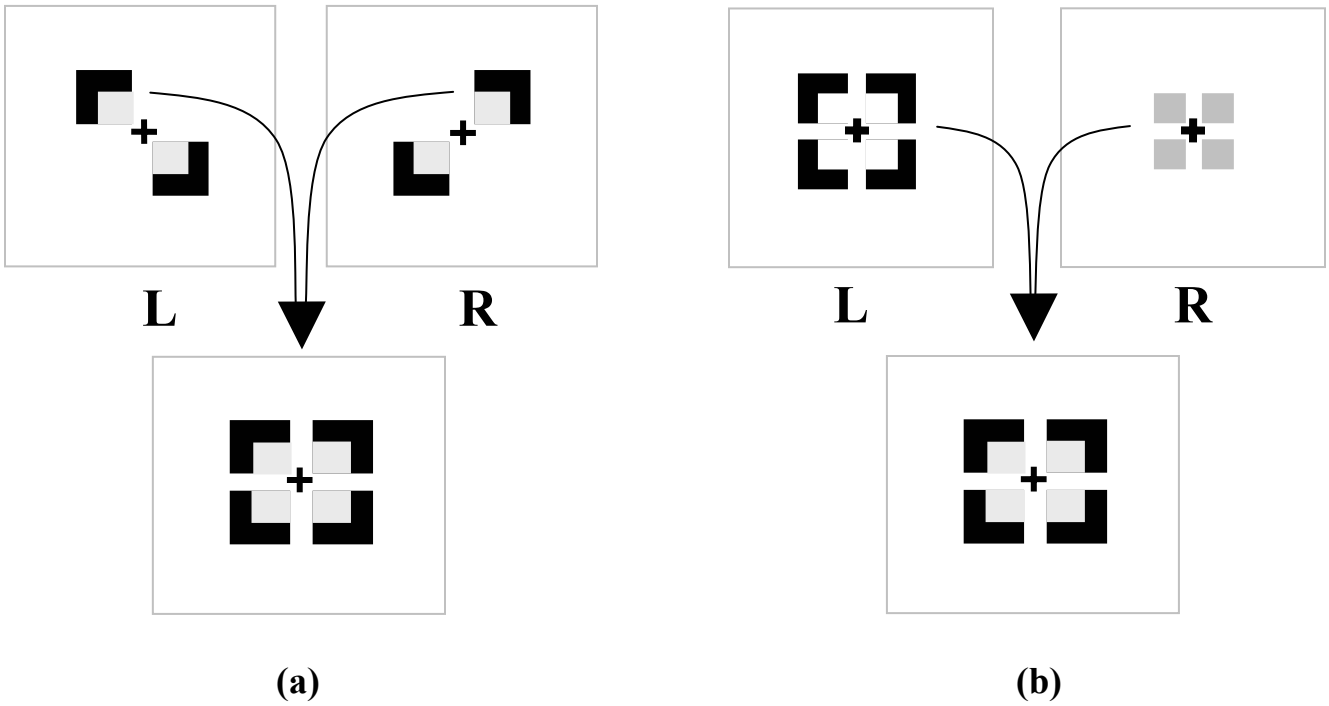

(a) (b)

Figure 4. (a) Splitting the inducers from Figure 2a across two eyes, while preserving the contrast relations within each eye, elicits neon color spreading. The illusory square bridges different ocularities. (b) When the contrasts of Figure 2a are split between the two images of the stereogram, then fusion of the stereogram does not yield neon color spreading.

To achieve this, the boundary grouping process pools signals from opposite contrast polarities at each position (Grossberg, 1994; Grossberg and Mingolla, 1985). In other words boundary grouping is *contrast-polarity invariant*.

How does the brain reconcile the coexistence of contrast-polarity sensitivity with contrast-polarity pooling for boundary formation? The 3D LAMINART model (Figure 1) unifies and functionally interprets many anatomical and neurophysiological data (Table 1), notably data concerning the laminar organization of V1 and V2, to propose an explanation of the data targeted in this article. The model proposes that contrast-invariant pooling occurs in layer 2/3A of V1 (Table 1, row 12) after like-polarity binocular fusion occurs in layer 3B (Figure 1; Table 1, rows 11 and 13).

1.6 Locating the monocular contrast constraint in V1 layer 4: A key prediction. Since V1 cells in layer 3B have already lost ocularity and are influenced by both eyes, we predict that the polarity-specific monocular process occurs before layer 3B of V1, notably in layer 4, where it can discriminate between the split contrast and the non-split contrast constraints in Tacheichi et al. (1992). The next sections show that this polarity-specific monocular process is monocular like-polarity competition.

	Connection in model (all in V1 unless otherwise noted)	Functional interpretation	Selected references
1	LGN→4	Strong, oriented LGN input	Blasdel and Lund (1983); Ferster *et al.* (1996, cat)
2	LGN→6	LGN input sharpened by 6→4 on-center off-surround	Blasdel and Lund (1983)
3	6→4 spiny stellates	Modulatory on-center of the 6→4 on-center off-surround	Stratford *et al.* (1996, cat); Callaway (1998)
4	6→4 inhibitory interneurons	Off-surround of the 6→4 on-center off-surround	McGuire *et al.* (1984, cat); Ahmed *et al.* (1997, cat)
5	4 inhibitory interneurons. → 4 inhibitory interneurons	Context-dependent normalization of off-surround inhibition	Ahmed *et al.* (1997, cat); Tamas *et al.* (1998, cat)
6	4→2/3 pyramidals	Feedforward of stimuli with bottom-up support	Fitzpatrick *et al.* (1985); Callaway and Wiser (1996)
7	2/3 pyramidals →2/3 pyramidals	Long-range collinear integration along RF axes	Bosking *et al.* (1997, shrew); Schmidt *et al.* (1997, cat); Tucker and Katz (2003a, b, ferret)
8	2/3 pyramidals →2/3 inhibitory interneurons	Keep outward grouping subthreshold (bipole property)	McGuire *et al.* (1991); Hirsch and Gilbert (1991, cat); Tucker and Katz (2003a, b, ferret)
9	2/3 inhibitory interneurons →2/3 inhibitory interneurons	Normalize 2/3 inhibition (2-against-1 part of bipole property)	Tamas *et al.* (1998, cat); Tucker and Katz (2003a, b, ferret)
10	V1 2/3 pyramidals →V2 layer 4	Feedforward of V1 groupings into V2	Van Essen *et al.* (1986); Rockland and Virga (1990)
11	Presence of simple cells and binocular cells in layer 3B of V1	Contrast sensitivity in layer 3B and obligate property	Dow (1974); Hubel and Wiesel (1968); Poggio,(1972); Katz *et al.* (1989)
12	3B → 2/3 in V1 and the presence of Binocular and complex cells in layer 2/3	Pooling responses of layer 2/3 of both contrast polarity from layer 3B	Callaway (1998); Poggio (1972)
13	Presence of cells in layer 3B and 2/3 that exclusively respond to binocular, not monocular stimulation	Obligate property	Poggio and Fischer (1977, rhesus); Smith et al. (1977); Poggio and Talbot (1981, rhesus); Poggio (1991)
14	Presence of moocular cells in layers 2 and 3	V1 monocular boundary formation	Poggio (1972); Hubel and Wiesel (1968)
15	V2 cells are mostly binocular	Model V2 cells (layer 4) input from both ocularities of monocular V1 cells (layer 2/3)	Hubel and Livingstone (1987); Roe and Ts'o (1997)
16	V2 cells are disparity-sensitive	Depth detection in V2	Poggio and Fischer (1977, rhesus); von der Heydt et al. (2000); Peterhans, (1997)
17	No false matches in V2	Disparity filter in V2	Bakin et al., 2000
18	Presence of false matches in V1	Depth propagation in model V1	Cumming and Parker (2000)
19	Presence of many complex cells in V2	Exclusive implementation of complex cells in the model V2	Hubel and Livingstone, 1987

Table 1. Neurophysiological and anatomical evidences for LAMINART

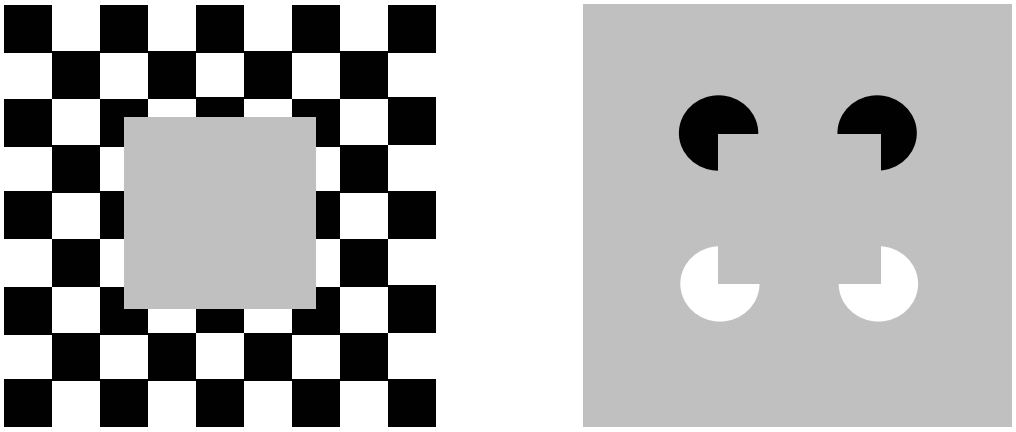

(a) **(b)**

Figure 5. (a) Boundary formation is contrast invariant: The polarity of contrasts along the square boundary reverses. However, these opposite contrasts are pooled by the brain to form the object boundary. (b) Long-range grouping to form the Kanizsa square pools over opposite contrast polarities.

2. 3D LAMINART circuit

Figure 1 summarizes how monocular polarity-specific competition is realized within the 3D LAMINART model. See the V1 circuit surrounded by the dashed line in Figure 1. Like-polarity binocular fusion occurs at binocular simple cells in layer 3B of V1 (Table 1, rows 11 and 13). Pooling of opposite contrast polarities occurs at complex cells in V1 (Table 1, row 12). Monocular and binocular signals are pooled at layer 4 of V2 (Table 1, row 15). A disparity filter also occurs in V2 to help solve the correspondence problem (Table 1, rows 16 and 17). Long-range contrast-invariant boundary completion, as in the Kanizsa square percept of Figure 5b, occurs in layer 2/3 of V2; see the V2 circuit surrounded by the dashed line in Figure 1 and Table 1 (rows 7, 8, and 9).

3. Contrast influences both boundary and surface processing

Because contrasts are pooled to form long-range boundary groupings (Figure 5b), thereby eliminating the possibility of distinguishing dark from light, they do not generate a visible percept within the boundary grouping system. Visibility is predicted to be a property of the surface filling-in system (Grossberg, 1994; Grossberg and Mingolla, 1985b). Interactions between the boundary and surface systems lead to the visible 3D surface percepts that are explained herein. An early stage in this interaction uses the depth-selective binocular boundaries that are formed in layer 2/3A of V2 (Figure 1) to selectively capture monocular surface signals at their depth (Figure 6, pathways 6). This surface capture process leads to a final percept of surfaces seen at different depths in V4. How this happens is described elsewhere to explain other data; e.g., Grossberg (1994, 1997, 2003), Grossberg and Swaminathan (2004), Kelly and Grossberg (2000). Here we review properties that are needed to explain the present data.

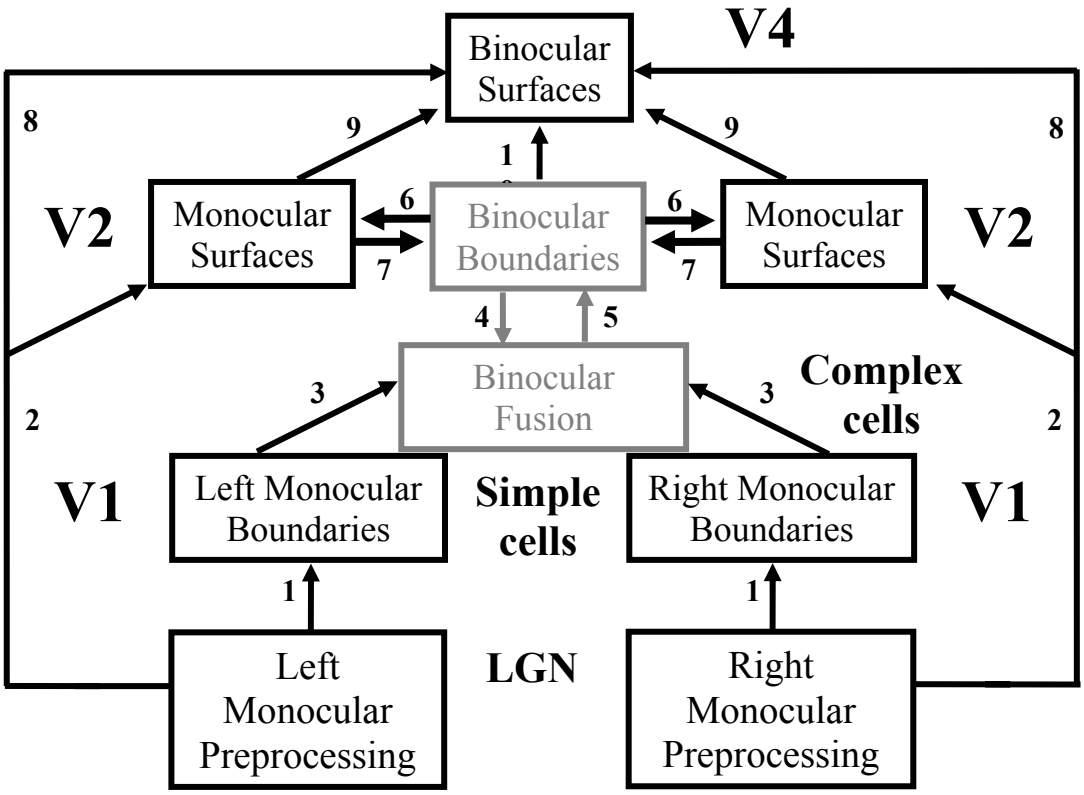

Figure 6. In FACADE theory, the illuminant-discounted inputs from Right and Left Monocular Preprocessing stage, which is composed of center-surround cells, output to the Left and Right Monocular boundaries composed of simple cells via pathway 1. This is the place where we suggest that like-polarity competition occurs (See Figure 1, V1 layer 4). Via pathways 3, Left and Right Monocular Boundaries are binocularly fused and through feedback via pathways 4 and 5 incorporate bipole long-range grouping which is provided by the Binocular Boundaries stage. Depthful binocular boundaries mutually interact with the Monocular Surfaces stage (pathways 6), where the closed boundaries are filled-in by the illuminant-discounted surface input. The attached boundaries to the successfully filled-in surfaces prune the corresponding boundaries at the farther depths at the same spatial positions (pathways 7). In the Binocular Surfaces stage, inputs from the Left and Right Monocular Preprocessing stages, and also the Left and Right Monocular Surface stages, are matched binocularly (pathways 8 and 9). The former match is based on excitatory inputs to the Binocular Surfaces stage and the latter match is inhibitory and carries out surface pruning. Binocular Boundaries are added to the same positions from near depths to far depths (pathways 10) to realize boundary enrichment. Due to surface pruning, the illuminant-discounted surface inputs associated with the enriched boundaries are pruned from the depths where boundaries are added (Pathway 9). The simulations in Figures 12 and 15 illustrate how these processing stages work.

One such property is that the illuminant is discounted (Figure 6, LGN stage) before the stage of depthful surface capture (Figure 6, Monocular Surfaces stage). This discounting process suppresses lightness and color signals within the interiors of regions with nearly uniform achromatic or chromatic contrast across space (Figure 7a). Contrasts are computed, with the illuminant discounted, at positions of rapid contrast change (Figure 6, LGN stage). These contrasts then fill-in surface regions within boundaries that inhibit, or gate, their spread (Figure 6, Monocular Surfaces stage). If the boundary corresponding to a surface border forms a closed contour, then it can contain the filling-in of surface lightness and color (Figure 7b). If the boundary has large gaps, then surface lightness and color can dissipate by spreading through the gaps (Figure 7c), thereby initiating the separation of surfaces in depth. We show how this happens by combining circuits in Figures 1 and 6 to explain the targeted data. The 3D LAMINART system (Figure 1) realizes the following stages in Figure 6: Left and Right Monocular Preprocessing (Figure 1, LGN), Left and Right Monocular Boundaries (Figure 1, Layers 6 to 2/3A leading to Monocular Complex Cells), Binocular Fusion (Figure 1, Binocular Simple Cells and Complex Cells) and Binocular Boundaries

(Figure 1, V2). The larger FACADE (Form-And-Color-And-DEpth) system in Figure 7 joins together boundary and surface processing.

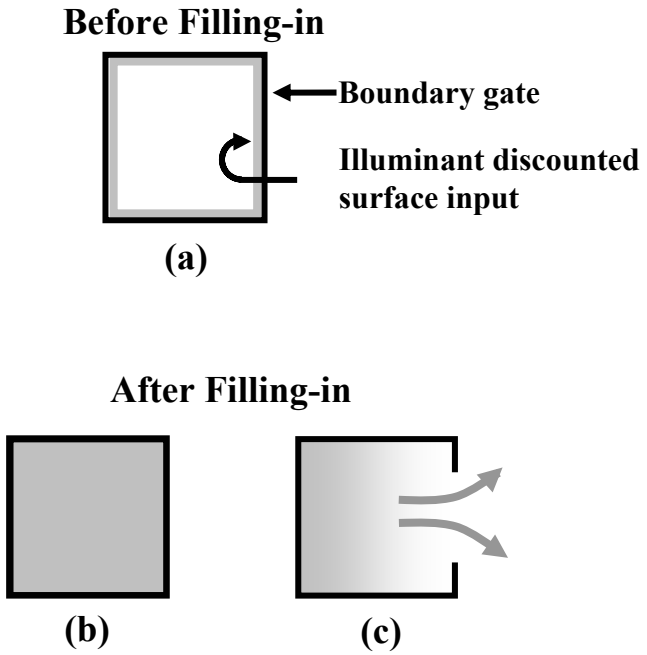

Figure 7. Each boundary output to the surface system is accompanied by illuminant-discounted surface inputs which estimate the contrast magnitude across the corresponding edge. (a) Before filling-in. (b) If the boundary does not have a gap, it then can contain filling-in and may lead to a visible surface percept. (c) A boundary with gap lets the filling-in dissipate, thereby preventing a visible surface percept.

4. How do surfaces and boundaries interact to cause transparency?

FACADE theory explains why a surface with a connected boundary is represented at a nearer depth than one with a boundary gap (Figure 8a): In response to viewing a 2D picture, the same boundaries initially form in several depth planes (Figure 9a) due to the size-disparity correlation (Kulikowski, 1978; Richards and Kaye, 1974; Schor and Tyler, 1981; Schor and Wood, 1983; Schor, Wood, and Ogawa, 1984; Tyler, 1975, 1983). A closed connected boundary in the BCS can contain filling-in within its surface region. A contrast-sensitive network is activated at the edges of such a filled-in region. This network sends feedback from surfaces to boundaries. The feedback is *positive* to the boundary at its own position and depth and *negative* to boundaries at the same positions but further depths (Figure 9b). Surface-to-boundary feedback confirms and strengthens the boundary that formed the surface region, while it inhibits, or prunes, any extra boundaries that form (Figure 9b). It hereby assures the consistency of boundary and surface representations.

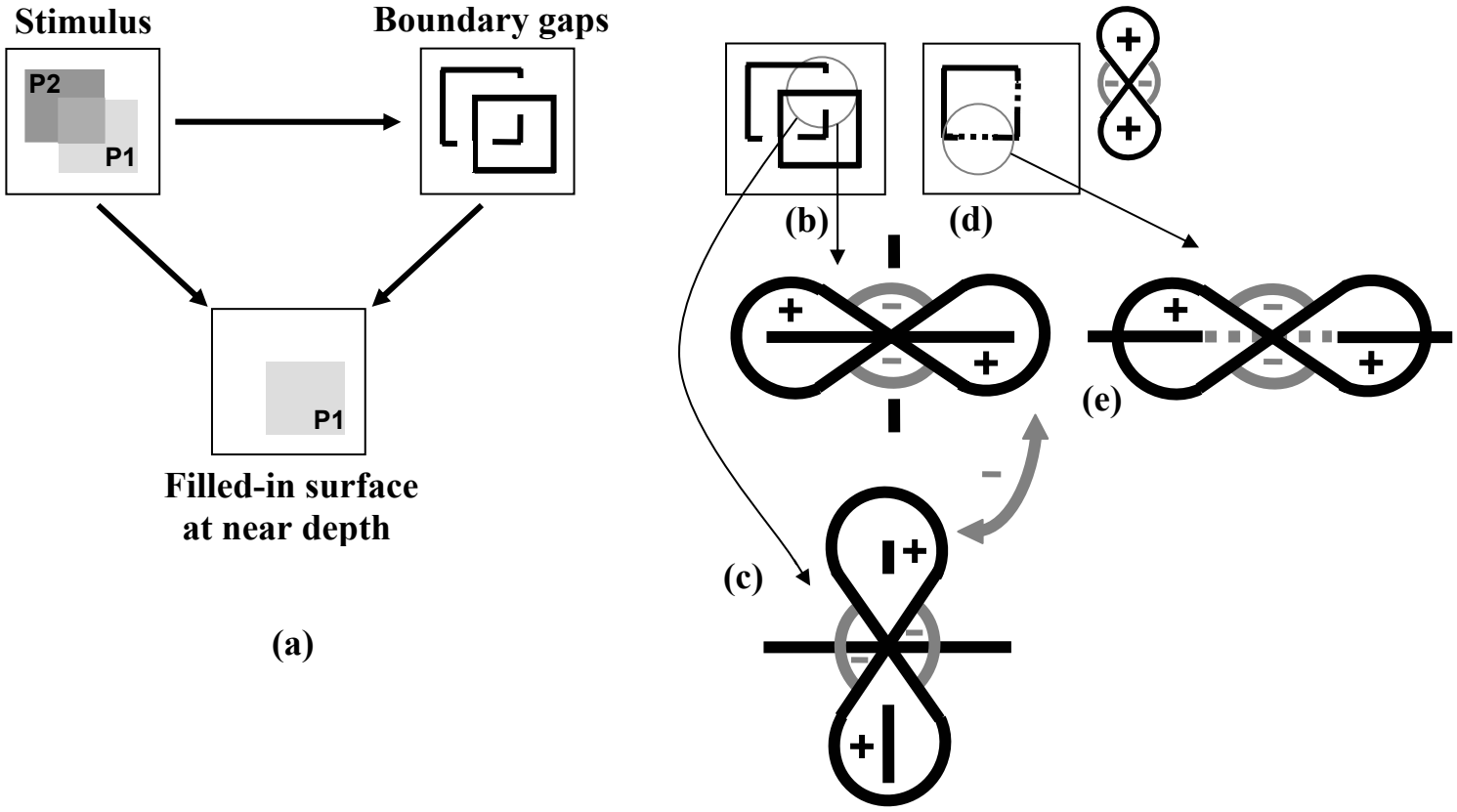

Figure 8. (a) In response to the stimulus, the intact boundary keeps its surface at the near depth and the surface presentation of the broken boundary will be forced behind (see Figure 9). How boundary gaps are generated and repaired: Panel (b) shows that in unique transparency, the underneath surface boundaries get gaps (within the circle) and as soon as the boundary signals across the gaps are pruned, the gaps can be repaired (see inside the circle). Panel (c) zooms into of the circle region of panel (b) to show how gaps can be created: The bipole grouping cells with different orientation preference (here orthogonal) compete. The stronger bipole inhibits the weaker bipole through orientational competition and causes gaps. The circle zone in (d) can be repaired because both lobes of bipole grouping cells get input (e). Before boundary pruning, the orthogonal boundary signal across the gap blocks the bipole grouping (b) both due to the activation of the inhibitory part of the bipole and also orientational competition as in (c).

When the boundaries of a near surface are inhibited at a far depth (Figure 9b), the boundary gaps at the far depth can be removed by collinear grouping, and the resultant closed boundary can contain surface filling-in of its illuminant-discounted input contrasts. In Figure 9b, the filled in surfaces at the near and far depths overlap, which corresponds to a percept of transparency.

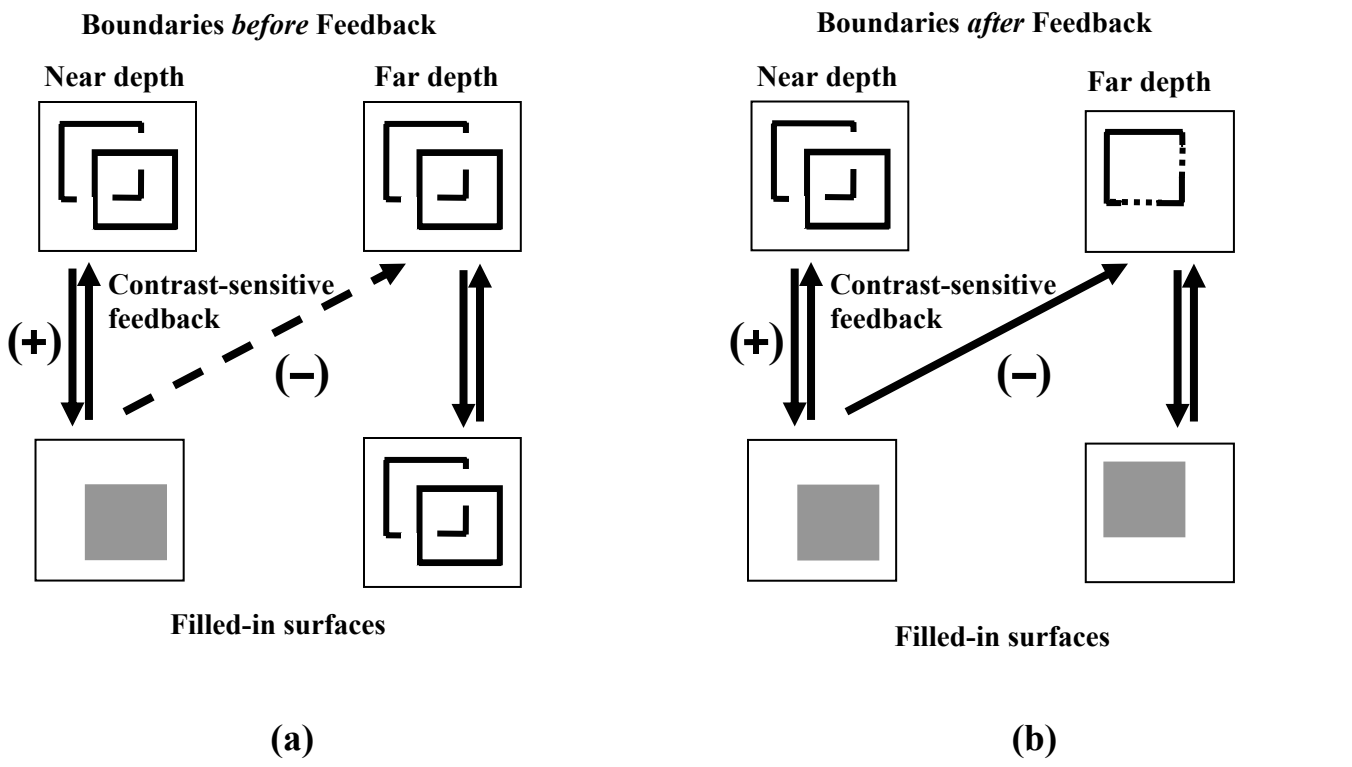

Figure 9. (a) Upper row shows that the initial boundary grouping is redundantly represented at several depths due to the size-disparity correlation. The successfully filled-in region will be assigned to the nearest depth that can create a closed connected boundary. Further boundaries at these positions are inhibited by contrast-sensitive topographic feedback from the successfully filled-in surface region. (b) Contrast-sensitive inhibitory feedback prunes the boundaries at further depths while strengthening the successfully filled-in boundaries at the near depth. Gaps in the occluded boundaries can then be repaired by collinear grouping.

The separated and completed boundaries and surfaces at the Monocular Surfaces stage in V2 enable us to recognize partially occluded objects. If these Monocular Surfaces were the ones that we see, however, then all occluders would look transparent (Grossberg, 1994). Visible 3D percepts are predicted to form at the Binocular Surfaces stage in V4 (Figure 6). The model hereby clarifies how the brain can *recognize* objects that are partially occluded by opaque objects, even though we can *see* only the unoccluded parts of these objects. It also explains when objects do look transparent. The distinction between seeing and recognizing is achieved by two mechanisms that act together: (1) adding boundaries at V2 to the surface representations at all further depths in V4 (*boundary enrichment*; pathways 10 in Figure 6); and (2) inhibiting monocular surface inputs to the surface representations at these farther depths (*surface pruning*; pathway 9 in Figure 6). As discussed below (Figures 12 and 15), these processes do not change the V2 boundaries and surfaces that form in the transparency and neon cases.

5. How are boundary gaps created and repaired?

Section 4 summarized how boundary gaps can lead to a transparent surface percept. Now we discuss how the monocular like-polarity competition enables these gaps to form, and how they are repaired. Perceptual grouping takes place in layer 2/3 of V2. The *bipole property* of such groupings can both generate boundary gaps and repair them by using a combination of long-range excitatory horizontal connections and short-range disynaptic inhibitory connections (Figure 1). The excitatory connections converge on a bipole cell from opposite sides, and enable it to complete illusory contours at positions that receive no bottom-up input. The inhibitory connections prevent such a boundary from forming unless there is convergent excitatory input from both sides. These inhibitory interactions also compete with boundaries that are trying to form with different, notably perpendicular, orientations at the same position. We will see below how monocular like-polarity competition assures that the boundaries of the

rightmost square in Figure 8b are stronger than those of the leftmost square. After competition across orientation (Figure 8c), the boundaries of the leftmost square are broken (Figure 8b). When contrast-sensitive surface-to-boundary feedback prunes the redundant boundaries of the rightmost square at the far depth (Figure 9b, far depth), the bipoles at the far depth no longer receive competition from the rightmost square. They can then collinearly complete the boundaries of the leftmost square (Figure 8d and 8e), which can then trigger filling-in of this square (Figure 9b), thereby leading to a percept of unique transparency.

6. Bipole grouping in V2 interacts with the monocular contrast constraint in V1

Why are the boundaries of the rightmost square in Figure 8b stronger than those of the leftmost square? The unique transparency image shown in Figure 10 shows that the contrast value at region A is larger than at region B. In addition, the contrast values at C and D can be nearly equal. In these cases, the average contrast of edge AC is larger than that of BD. How, then, does the bipole whose lobes are on BD win over those on AC, as required by Figures 8 and 9?

Something more must happening to generate the proper boundary gaps, other than bipole grouping. Although the average contrast of edge AC is larger than that of BD, the contrast polarity of edge A is the same as that of the edge C, whereas the contrast polarities of B and D are opposite. Monocular polarity-specific competition in V1 therefore weakens the AC boundary, but not the BD boundary. As shown below, the competition weakens the amplitudes of inputs to the AC bipoles, but not the BD bipoles, in V2. This additional property, when combined with the other properties summarized in Figure 8 and 9, suffices to explain all of our targeted data about transparency and neon color spreading.

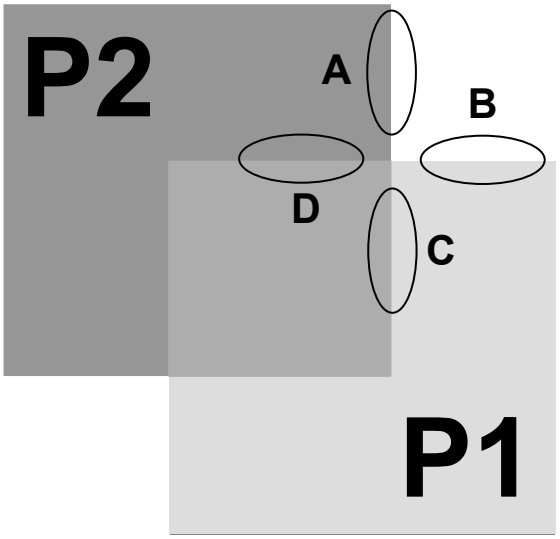

Figure 10. Boundary BD can win over AC even if contrast AC > BD to keep the transparent surface in front. Consider Figure 12 for the solution of this "absolute value problem".

7. Prediction: Monocular polarity-specific competition occurs in V1 layer 4

We propose that the monocular polarity-specific competition occurs among simple cells of layer 4. Each layer 6 simple cell in Figure 1 directly excites the corresponding layer 4 simple cell with the same contrast polarity (see also Table 1, row 3) and indirectly inhibits it via the inhibitory interneuron (Table 1, row 4). Because excitation and inhibition are approximately balanced within the on-center of the layer 4 cell, with the excitation possibly a little stronger, net excitatory modulation by layer 6 of its layer 4 on-center can occur. The layer 4 cell is also activated to suprathreshold values by direct LGN inputs (Table 1, row 1). In addition, off-surround inhibition from layer 6 to layer 4 extends to the coaxial flankers of

layer 4 simple cells that have the same polarity response; see also Table 1, row 4. We predict that the latter circuit embodies monocular polarity-specific competition.

As noted above, in the unique transparency stimulus of Figure 10, A and C have the same contrast polarity, hence they compete, so the simple cell activities in this region become weaker. Because regions B and D have opposite contrast polarity, they do not compete. Their corresponding simple cell activities are actually stronger than in the case that either boundary B or D would have continued uniformly without crossing a junction. This is because a uniform edge has the same polarity of contrast along its border, which activates the same-polarity competition pathway. The reversal of polarity from B to D frees the corresponding simple cells from continuous edge-induced inhibition and thereby makes the boundary signal around the junction zone stronger than in the case wherein a uniform edge continues. This strong BD boundary can win the orientational competition over the weakened AC boundary at the bipole cells in V2, despite the fact that the average absolute contrast of AC is greater than that of BD. The Results section will also show that these mechanisms correctly stratify the bistable and nontransparent cases.

The same mechanisms are sufficient to explain data about neon color spreading or blockade. Figure 11a shows that the desired situation is the winning of the bipole grouping along AC over BD even if the average contrast value along BD is greater than AC (note around C, there is no contrastive edge). Monocular polarity-specific competition helps to solve this problem: Boundary A is freed from same polarity-specific competition because it ends after crossing BD, and thereby gets even stronger. However, there is polarity-specific competition within BD. The strengthening of A through discontinuation and the weakening of BD through polarity-specific competition enable bipoles which form an illusory contour by grouping AC to win over BD through orientational competition.

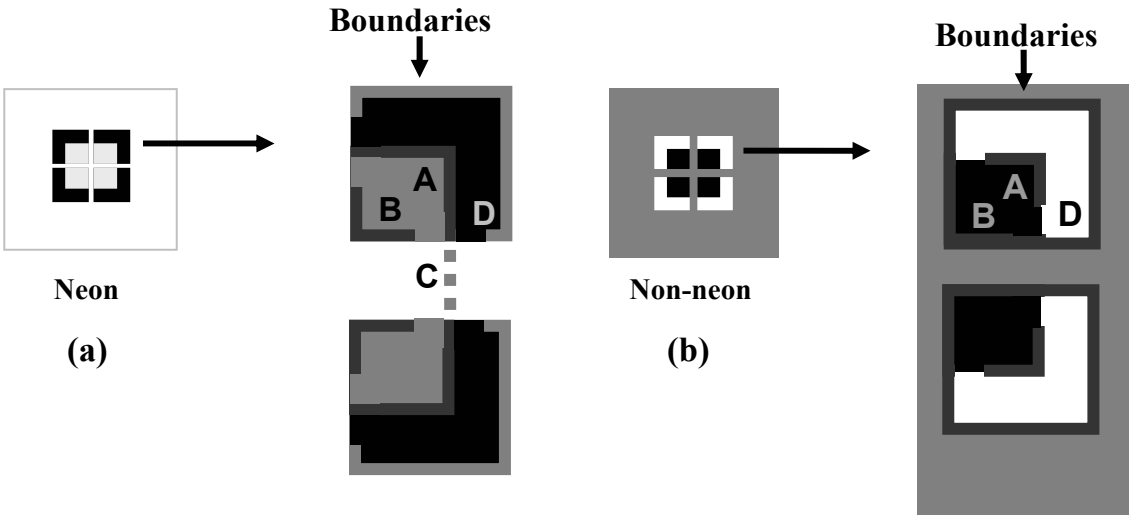

Figure 11. Neon and no-neon cases: Boundary AC can win even when contrast D exceeds contrast A. Polarity-specific competition between B and D allows boundary AC to win. (b) Boundary BD can win even when contrast A exceeds D. Opposite-polarity B and D contrasts do not compete. Boundaries are shown schematically as grey edges.

The same sort of hypothesis can successfully explain the blocked neon case of Figure 11b: Boundary BD uses its bipole grouping advantage to win even if the contrast value at A is greater than at D. This is because opposite polarities B and D do not compete.

The prediction of like-polarity competition is consistent with data of Polat and Sagi (1993), in which the detection threshold of a Gabor patch flanked by two patches with the same contrast polarity increases when the flankers get nearer to the target. In their experiment, the flanker contrasts were in phase with the target contrast, equivalent to a like-polarity condition. It remains to be tested via direct recording in V1 what happens if the flanker contrast and the target contrast are spatially out of phase. One has to be cautious even to draw the conclusion that in the out-of-phase case, or opposite polarity

case, the raised threshold effect will be less, because polarity-pooled cells of V2 (among other cells) may modulate the predicted V1 effects.

8. Same ocularity of contrast can induce neon

The combination of monocular polarity-specific competition in V1 and binocular contrast-invariant bipole grouping in V2 can also explain the Takeichi et al. (1992) data. In the no-neon case of Figure 4b, the different ocularity of the contrasts bypasses the monocular polarity-specific competition in V1. The same polarity (gray-white) of the right panel is thus not adjacent to the same polarity (black-white) of the left panel to activate this competition. In the neon case of Figure 4a, monocular polarity-specific competition contributes to boundary gap formation in favor of the long-range bipole cooperation that completes the illusory square. The illusory square can form between inducers with different ocularities because layer 2/3 bipole grouping cells in V2 are binocular (Figure 1). Taken together, the endgaps and binocular illusory contours can support the neon effect, as simulated below.

9. Simulation results

9.1 Simulation of unique transparency. For simplicity, the present simulations contain only two depth planes: Near and far. Initially, the same boundaries occur in both depth planes (Figure 12a and Appendix sections A4-A8). As described in Figure 9a, the boundary of the rightmost square is intact and of the leftmost square has gaps. Surface filling-in is contained within the connected boundary and flows out of the gaps in the broken boundary (Appendix sections A9-A12). Figure 12a shows the situation before the contrast-sensitive feedback takes place from the connected near surface to the far depth boundaries (Appendix sections A7 and A10). 3D LAMINART simulations of 3D planar surface percepts with more depth planes in Grossberg and Howe (2003) and Grossberg and Swaminathan (2004) show that the present simplification generalizes.

Figure 12b shows that the analysis in Figure 9b works; namely, after contrast-sensitive surface-to-boundary feedback in V2, the far boundary of the successfully filled-in near surface is pruned. This frees the bipole grouping kernels to repair the remaining far boundary gaps (Figure 12b and Appendix section A8). Now surface filling-in at the far depth can be contained in this closed boundary.

In Figure 12c, the processes involved in the Binocular Surfaces stage in V4 are shown. The near depth replicates the boundary and filled-in surface of Figure 12b; see Figure 12c. However, the situation at the far depth in V4 differs from that in V2 (compare Appendix sections A9 and A12). In the leftmost panel of Figure 12d, the boundary of the successfully filled-in surface at the near depth is added to the boundary at the far depth (boundary enrichment). In addition, the surface inputs corresponding to the far boundaries are pruned from the far depth (surface pruning). In the rightmost panel, the resultant surface and boundary interaction within the Binocular Surfaces stage is shown. As can be seen, the weaker contrast of the lower-right part of the square. Along with the separation of this part from the rest of the square by the boundary enrichment process, result in a weaker surface activity (rightmost panel of Figure 12d). The latter surface activity is behind the near surface, hence gives rise to the transparency percept again. This weaker contrast illustrates how contrasts can be stratified across multiple depths.

9.2 Bistable transparency simulation. In the bistable transparency case (Figure 2b), both stems of the X-junction preserve polarity. Due to polarity-specific competition (Appendix section A3), both generate weak boundaries. If the contrasts of both X-junctions are balanced, then their bipoles (Appendix section A8) cannot generate boundary gaps. Then the image in Figure 2b may result in a non-stratified percept with a small square in the middle and two flanking L shapes. However, if attention shifts between the edges of the X-junction, or their corresponding surface regions, then bistable endgaps and bistable transparency can occur, because attention can favor one of the boundaries. Attention is simulated as top-down Gaussian activation to layer 6 of V1 (Figure 13c, Appendix section A1c). Layer 6, in turn, positively modulates layer 4 activation (Figure 13c, Appendix section A3). Activation of layer 4 in favor of any boundary enables it to win the orientational competition (Appendix section A6) and to push its surface to the near depth plane.

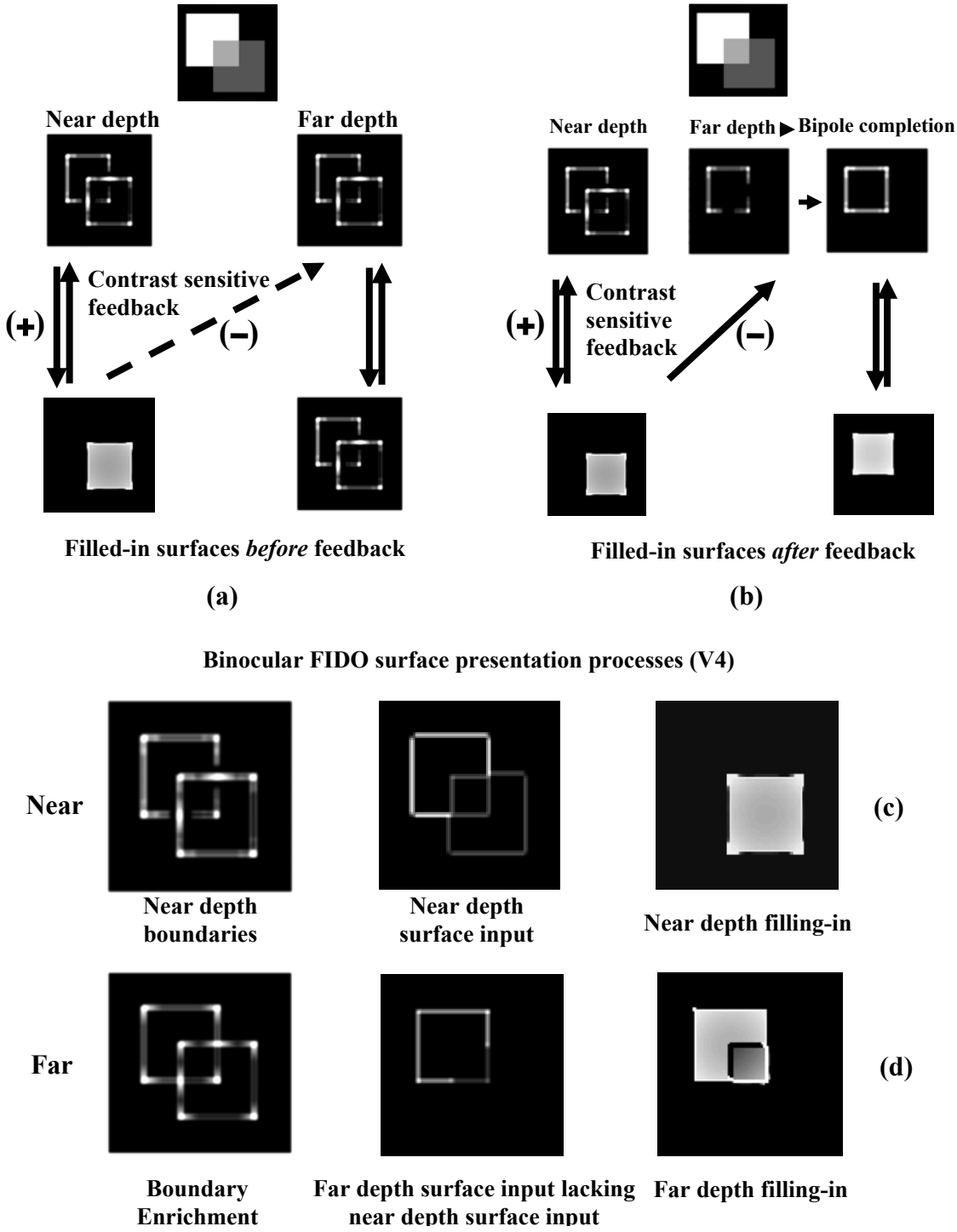

Figure 12. (a) Before boundary pruning occurs from near-to-far, the boundary gaps in the far depth cannot be repaired. (b) After far depth boundary pruning occurs, the repaired gaps close the square boundary and allow it to contain the filling-in process. (c) The binocular FIDO stage (V4) from left to right: The near depth connected boundaries are added to the far depth boundaries. The middle panel shows that the corresponding surface inputs related to the enriched boundaries are pruned from the far depth. The right panel shows the surface filling-in of the far depth. See the text for full description.

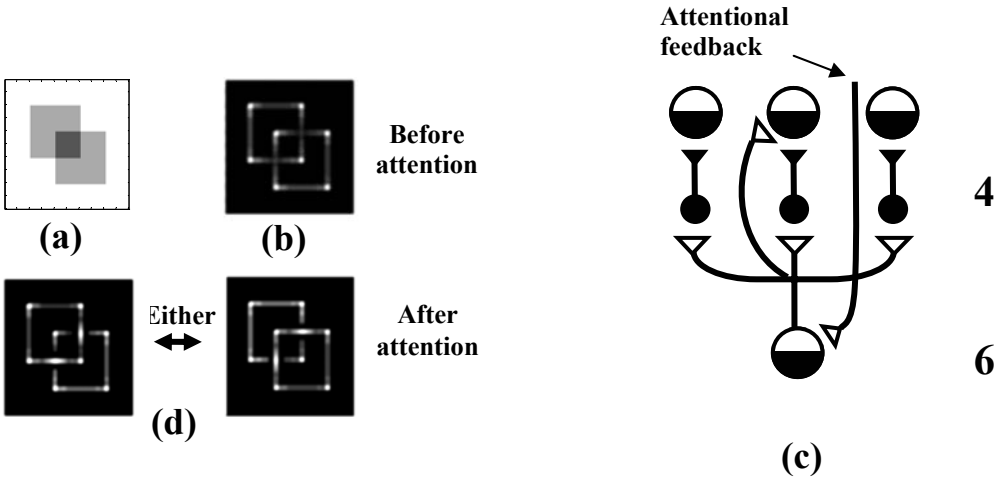

Figure 13. In the bistable transparency case (a), the same polarity along both stems of the X-junctions makes their boundaries weak and unable to win over the other (b). Positive modulatory attentional feedback (c) to either of the stems makes it win over the other (d). See the text for details.

9.3 Non transparent simulation. A double polarity-reversing X-junction (Figure 2c) generates strong boundary signals around X-junctions. Orientational competition here too cannot generate gaps along either of them. Because both stem boundaries are strong due to the lack of polarity-specific competition, subliminal attentional boundary enhancement in favor of either stem cannot make it win over the other one, consistent with the greater effect of attention on weak than strong groupings.

The illuminant-discounted surface input successfully fills-in all the closed contours, so contrast-sensitive surface-to-boundary feedback (Appendix sections A7 and A10) prunes all the boundary copies in the far depth; hence, no boundary signals remain there. All surfaces hereby form in one depth plane with no surface representation behind the overlap region, as shown in Figure 14, so there is no percept of transparency.

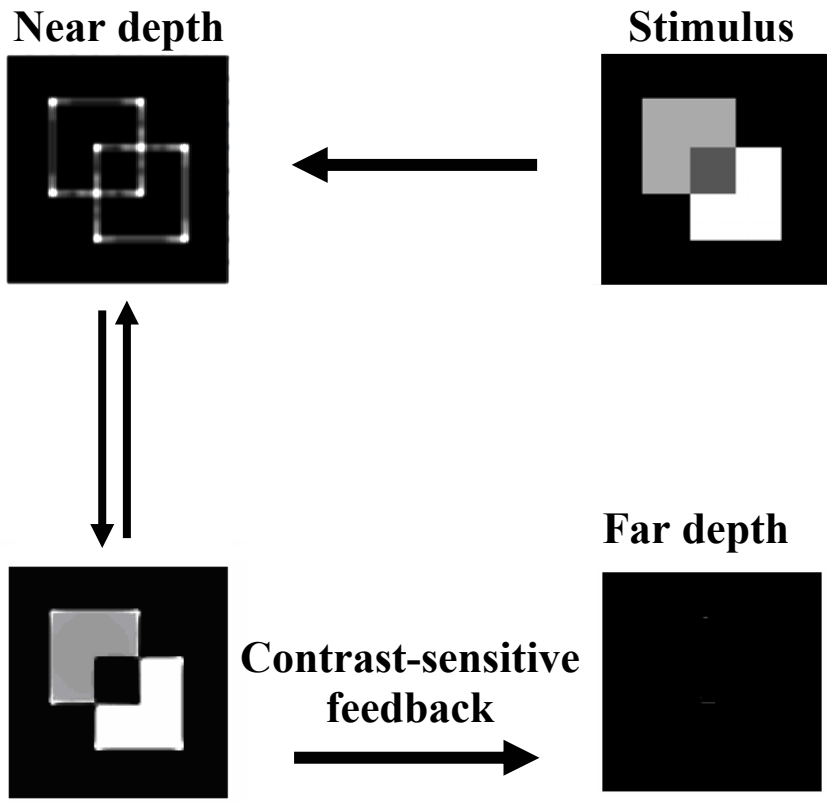

Figure 14. In the non-transparency case, polarity reversal along both stems of X-junction leads to strong boundaries Xthat can resist orientational competition. Attention to either boundary cannot break the other strong stem. Therefore, all closed boundaries are filled-in at the same depth plane. See text for more details.

9.4 Neon simulation. In the neon case of Figures 3a and 15a, monocular like-polarity competition (Appendix section A3) enables the illusory square to form, as was proposed in Figure 11a. The illusory square interpolates the boundary gaps. A square surface fills-in at the near depth plane. Then contrast-sensitive surface-to-boundary feedback prunes the square boundary from the far depth plane. Boundary completion can then form four small square boundaries at the far depth plane, which can then fill-in.

The simulation clarifies the perceptual experience that the surface quality of the neon is pretty weak. In the simulation, feature contrasts occur at the four small gray square corner inducers of the illusory square. The illusory parts of the square sides do not have any surface input, because there are no contrastive edges there. These sparse inducers spread throughout the entire illusory square. This is unlike the transparency case in which the surface input exists along the whole edge of the square.

In Figure 15b, the simulation of the Binocular Surface stage (Appendix section A12) is shown. The leftmost panel shows the boundary enrichment at the far depth. The surface inputs corresponding to the near connected boundaries are pruned from the far depth surface input (middle panel). The filling-in of the pruned surface input within the enriched boundaries is shown in the right panel. The far depth surface representation is not different qualitatively at the Monocular and Binocular Surfaces, because the small corner square surface inputs are intact at the far depth after surface input pruning.

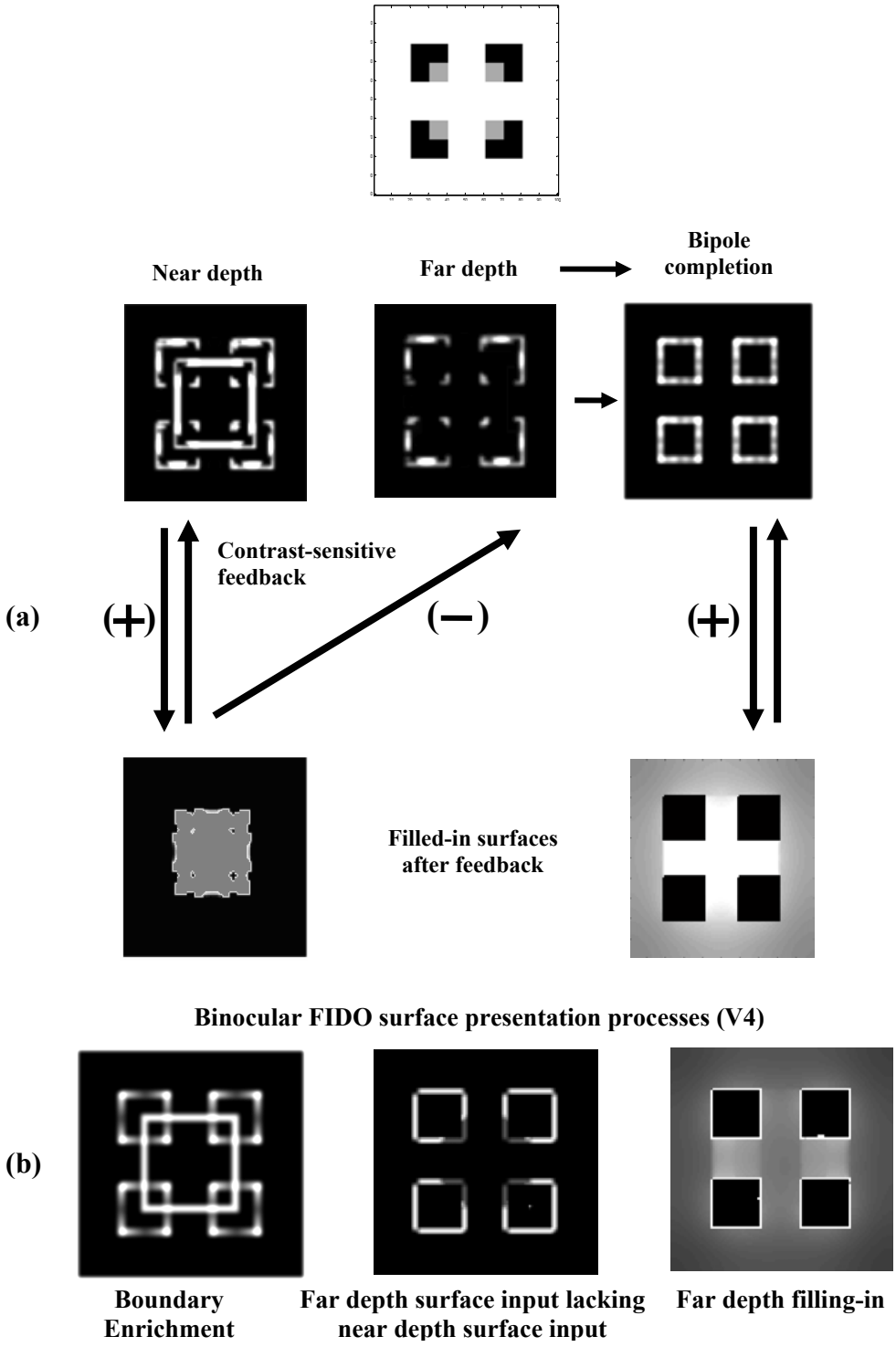

Figure 15. (a) In the neon case, the preserved polarity along the T-junction tops weakens the top boundary signals and enables boundary gaps to form via orientational competition. These gaps create a suitable condition for long-range grouping whereby the middle square illusory boundary forms. This middle square fills-in successfully and after pruning the corresponding boundaries from the far depth, four small square boundaries are repaired by long-range grouping after being released from orientational competition by the middle square boundaries. Filling-in of the four squares can then occur behind the middle square. (b) Left panel shows that, at the binocular FIDO stage, the connected boundaries of the successfully filled-in surface at near depth are added to the boundaries at the far depth (boundary enrichment). The surface inputs corresponding to the enriched boundaries are removed from far depth via surface pruning (middle panel). The surface filling-in within the enriched boundaries by the pruned surface input represents the four corner squares at the far depth (right panel).

9.5 Non-neon simulation. Figure 16 shows the effect of polarity reversal along the T-junctions in strengthening the boundaries corresponding to the top of the T-junction, and in not allowing the perpendicular bipole grouping to take place, as schematized in Figure 11b. As a result, the whole surface representation is on one depth plane, much as in the non-transparent simulation in Figure 14.

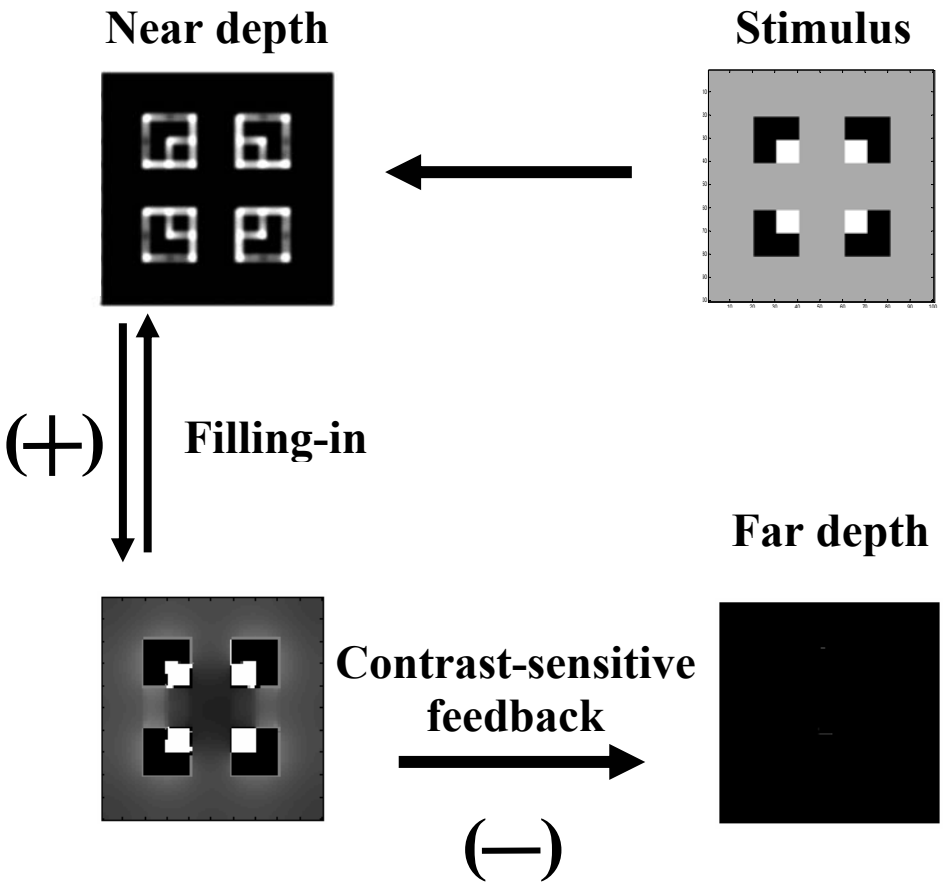

Figure 16. In the non-neon case, opposite polarities along the tops of the T-junctions strengthen the top boundaries, which in turn block the long-range grouping by orientational competition.

9.6 Dichoptic neon simulation. In the neon split case (Figure 4a) because the whole contrast exists within each monocular inducer, suitable boundary gaps will be generated and binocular long-range grouping can bridge between inducers with the opposite ocularity (Figure 17). The rest of the process is the same as in the neon case of Figure 15.

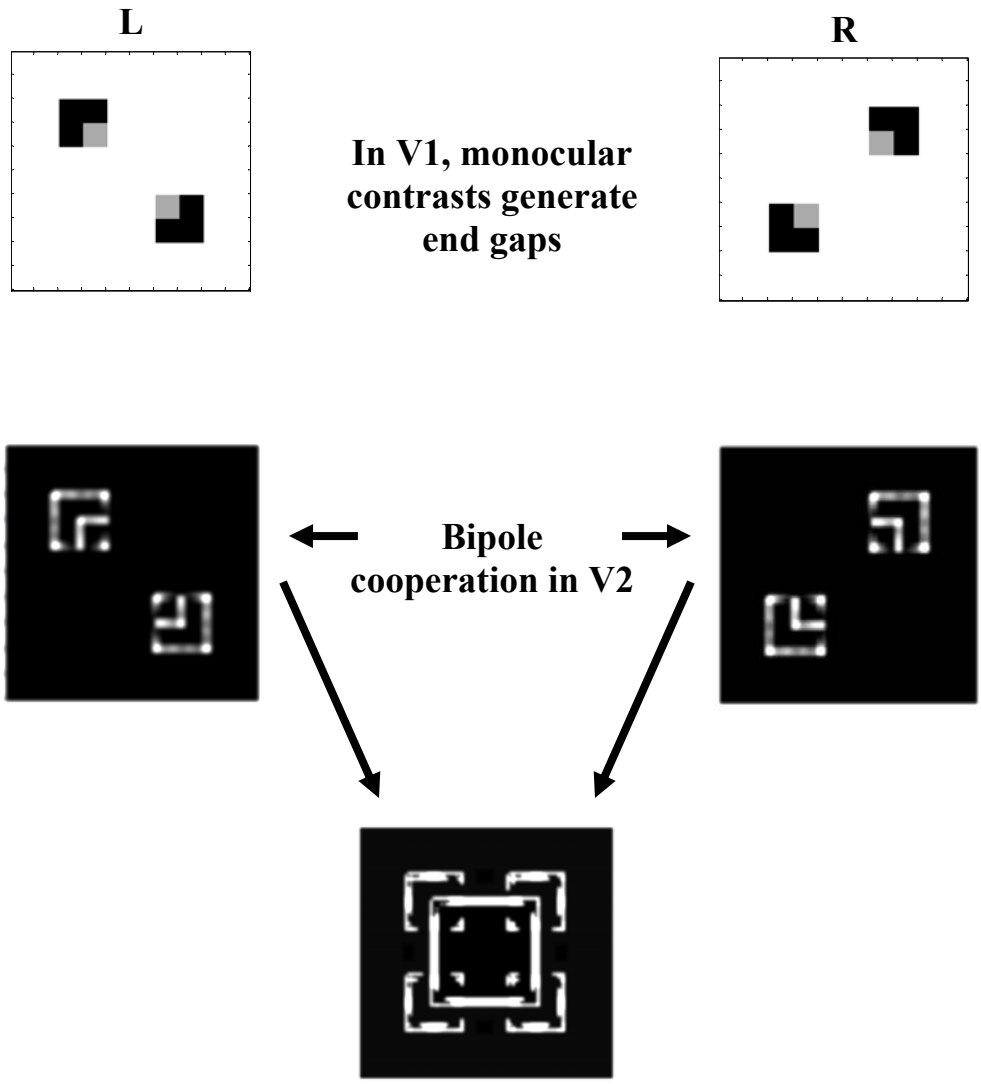

Figure 17. In the dichoptic neon case, the presentation of the whole contrast to each eye generates boundary endgaps. Due to the binocularity of long-range grouping, the middle illusory square boundary can form. Hence neon can be generated. See text for details.

9.7 Dichoptic non-neon split contrast simulation. Due to the different ocularity of the contrast components in this case (Figure 4b), the boundaries around the line ends get stronger. The pooling of polarity and ocularity at layer 2/3 of V2 (Appendix section A8) results in strong boundary signals perpendicular to the orientations of the illusory square that forms in the neon case. Orientation competition (Appendix A8) prevents boundary gaps and illusory contour formation from occurring (Figure 18).

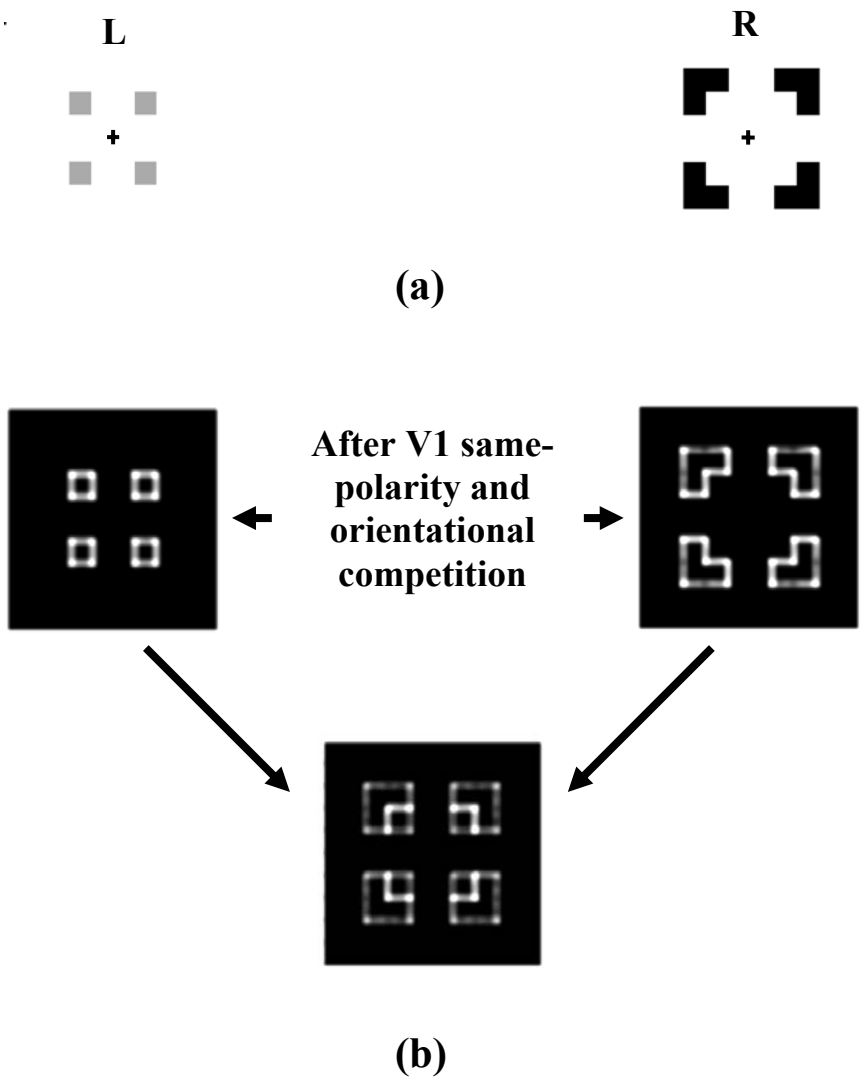

Figure 18. In the dichoptic non-neon case, the different ocularity of the contrast components (a) bypasses the polarity-specific competition so that no endgaps are formed (b). Binocular long-range grouping to form a middle illusory square is blocked by strong perpendicular boundaries (b). See text for details.

10. Discussion: Supportive data and new predictions

10.1 Physiological and anatomical data that support the model. Neurophysiological and anatomical data support every processing stage of the model (Table 1), including its laminar interpretation. The model does not include cortical areas V3 and V3A, which are known to be involved in depth perception (Backus et al., 2001; Tsao et al., 2003). These areas are not required to simulate the present data. The function of area V3A is controversial. Studies propose that it is variously involved in relative disparity (Backus et al., 2001), saccades (Nakamura & Colby, 2000a, 2000b) and grasping hand movements (Nakamura et al, 2001). As a further complication, there is evidence showing that the function of macaque V3A is different from that of human V3A (Tootell et al., 1997). These areas may be required when the present model is combined with mechanisms for looking, reaching and grasping.

10.2 Predictions and the explanatory power of the model. All of the model processing stages have explicit neural labels, so their functional properties constitutes testable predictions. Many such predictions have been tested with positive results; see Dresp and Grossberg (1997), Dresp and Grossberg (1999), Dresp, Durand, and Grossberg (2002), Howe (2001), Howe and Watanabe (2003), Raizada and Grossberg (2003), and Yazdanbakhsh and Watanabe (2004) for recent examples.

The stimuli that generate transparency and neon color spreading are rare in natural conditions, but they illuminate constraints on visual system strategies for depth stratification that have evolved in natural environments. In particular, the monocular like-polarity constraint is predicted to be realized in the monocular circuits of layers 6 and 4 of V1. The model shows how this constraint coexist with the facts that long-range grouping can pool over opposite contrast polarities and in response to dichoptic inputs. The latter properties are realized by layer 2/3 of V2.

The long-range grouping process in layer 2/3 of V2 has a clear ecological value; see Figure 5. Can the same be said for monocular polarity-specific competition in layer 6-to-4 of V1? Earlier analysis has shown that the layer 6-to-4 competition has at least three useful functions (Grossberg, 1999a): (1) It contrast-normalizes the responses of layer 4 cells to bottom-up inputs; (2) it assures that the correct groupings are selected via layer 2/3-6-4-2/3 feedback without losing their analog sensitivity to inputs; and (3) it maintains an approximate balance between excitation and inhibition in the layer 6-to-4 on-center that enables top-down attention to modulate layer 4 cells, as in Figure 13c. These properties do not, however, require the polarity-specificity of layer 4 competition. How does this constraint arise? Grossberg and Williamson (2001) simulated how the layer 6-to-4 competition and the layer 2/3 long-range grouping connections develop. Their study showed how the approximate balance between excitation and inhibition in the layer 6-to-4 on center could develop, and that, if the excitation or inhibition got too strong, then model development did not stabilize.

The developmental and learning laws that achieve the desired stabilizing balance also create an inhibitory kernel around layer 4 cells that links cells which code the same collinear orientation, since "cells that fire together wire together". Under natural viewing conditions, objects typically have the same orientation *and* the same contrast polarity for a considerable distance along their edges. One would therefore expect monocular like-polarity inhibitory kernels to develop.

This analysis leads to new experimental questions and predictions that link properties (1)-(3) above with issues about developmental stability and transparency. In particular, what happens to these inhibitory kernels if animals are reared in an artificial environment composed of textures whose polarities reverse at frequent intervals across space? Do these animals develop inhibitory kernels that violate the like-polarity constraint? Do relative contrast differences *per se* then determine their percepts? Do they see transparency and neon percepts differently than we do?

When the like-polarity constraint is realized within the 3D LAMINART model, it provides a mechanistic explanation of the classical Metelli rules for when a transparent percept will be generated. In particular, Beck, Prazdny, and Ivry (1984) and Metelli (1974) showed that transparency occurs when (1) "the overlying of the transparent surface does not change the order of the lightness values", and (2) "the lightness difference within the transparent area must be less than the lightness difference outside the

transparent area". Because of like-polarity competition, constraint (1) can break the boundary of the non-transparent surface and leave the transparent one intact. Like-polarity competition supplemented by orientational competition (Appendix section A8) generates a larger gap on the boundary of the non-transparent surface inside the transparent area than outside of it if constraint (2) is obeyed. The larger gap leads to a more uniform spreading of surface activity within the transparent area. This is consistent with the percept: The overlaying transparent surface has a uniform surface quality.

Appendix: 3D LAMINART Equations

In the LAMINART circuit shown in Figure 1, total excitatory and inhibitory inputs to each cell can be represented, respectively, by time-varying conductances $\gamma_{ex}(t)$, and $\gamma_{inh}(t)$ in a membrane equation with a constant leakage conductance γ_{leak} (voltage-independent conductance equal to: $\frac{1}{\text{Resistence}}$) and reversal potentials for excitation E_{Ex} (corresponding to Na^+ channels), inhibition E_{Inh} (corresponding to K^+ channels), and leakage (E_{Leak}). Then the membrane potential $V(t)$ can be written as:

$$C\frac{dV(t)}{dt} = -[V(t)-E_{Ex}]\gamma_{Ex}(t) - [V(t)-E_{Inh}]\gamma_{Inh}(t) - [V(t)-E_{Leak}]\gamma_{Leak}(t), \qquad (1)$$

where C is the conductance of the cell membrane.

In many parts of the simulation, (1) is solved at equilibrium. At equilibrium, the above equation becomes:

$$V = (E_{Ex}\,\gamma_{ex} + E_{Inh}\,\gamma_{inh} + E_{Leak}\,\gamma_{inh}) / (\gamma_{ex} + \gamma_{inh} + \gamma_{inh}). \qquad (2)$$

The denominator in (2) shows how the membrane potential is normalized divisively. In the subsequent simulations, $E_{Ex} = 1$, $E_{Inh} = -1$, $E_{Inh} = 0$, $\gamma_{ex}(t)$ and $\gamma_{inh}(t)$ are replaced by total excitatory and inhibitory signals, respectively. The resultant differential equations are then solved either in equilibrium or by the forward Euler method with the time step of 0.05 ms in MATLAB. The surface filling-in simulations are written in C++ as a MEX file incorporated into MATLAB to make the run time faster. Equations that were solved at equilibrium are written below in the form (2).

A1. Retinal/LGN processing and outputs to V1. Notation $I_{pq}^{L/R}$ denotes the visual input to the lumped retina and LGN processing stages of the left (L) or right (R) eye at location (*p,q*). Contrast-sensitive ON cell activity $x_{ij}^{L/R+}$ obeys an on-center ($C_1^{L/R}$) off-surround ($S_1^{L/R}$) membrane equation:

$$\frac{dx_{ij}^{L/R+}}{dt} = -x_{ij}^{L/R+} + (U_1 - x_{ij}^{L/R+})C_{ij}^{L/R} - (x_{ij}^{L/R+} + L_1)S_{ij}^{L/R}. \qquad (3)$$

Contrast-sensitive OFF cell kernels are reversed (Grossberg and Kelly, 1999):

$$\frac{dx_{ij}^{L/R-}}{dt} = -x_{ij}^{L/R-} + (U_1 - x_{ij}^{L/R-})S_{ij}^{L/R} - (x_{ij}^{L/R-} + L_1)C_{ij}^{L/R}, \qquad (4)$$

where $C_{ij}^{L/R} = \left[\sum_{pq} I_{pq}^{L/R} C_{pqij}^{(k)}\right]^+$, $S_{ij}^{L/R} = \left[\sum_{pq} I_{pq}^{L/R} S_{pqij}^{(k)}\right]^+$, and the kernels $C_{pqij}^{(k)}$ and $S_{pqij}^{(k)}$ are Gaussian.

ON and OFF cells compete to yield the following ON and OFF output signals to V1:

$$X_{ij}^{L/R+} = \left[x_{ij}^{L/R+} - x_{ij}^{L/R-}\right]^+, \qquad X_{ij}^{L/R-} = \left[x_{ij}^{L/R-} - x_{ij}^{L/R+}\right]^+. \qquad (5)$$

These output signals give rise to oriented and polarity-sensitive inputs $S_{ijk}^{L/R} = [\sum_{pq} X_{ij}^{L/R+} D_{pqij}^{(k)}]^+$ to V1 from LGN, at V1 position (*i,j*) and orientation *k*, originating from the left (L) or right (R) eye, where kernel $D_{pqij}^{(k)}$ is defined by a difference-of-shifted-Gaussians.

A2. Layer 6 of V1

Cell activity $x_{ijk}^{(1,L/R)}$ of layer 6 of V1 at position (*i,j*) with left/right (L/R) ocularity and orientation index *k* is given by:

$$\frac{d}{dt} x_{ijk}^{(1,L/R)} = -x_{ijk}^{(1,L/R)} + (1 - x_{ijk}^{(1,L/R)})(S_{ijk}^{L/R} + \sum_{pq} A_{ij}^{pq}). \tag{6}$$

The attentional feedback term $\sum_{pq} A_{ij}^{pq}$ in (6) is defined by the summation of Gaussian kernels.

$$A_{ij}^{pq} = \frac{1}{2\pi\sigma^2} \exp\left(-\frac{1}{2} \left(\frac{(p-i)^2 + (q-j)^2}{\sigma^2} \right) \right). \tag{7}$$

Attention is used only in the bistable transparency case; see Figure 16. In cases with no attentional feedback, $A_{ijk}^{pq} = 0$. In the bistable transparency case, attention is focused at positions (*p,q*) which are along either stem of X-junctions. At equilibrium, (6) becomes:

$$x_{ijk}^{(1,L/R)} = \frac{S_{ijk}^{L/R} + \sum_{pq} A_{ij}^{pq}}{1 + S_{ijk}^{L/R} + \sum_{pq} A_{ij}^{pq}}. \tag{8}$$

In both (6) and (8), $x_{ijk}^{(1,L/R)}$ is contrast-polarity sensitive.

A3. V1 layer 4: Monocular simple cells

The monocular simple cell activity of layer 4, $y_{ijk}^{(1,L/R)}$ is given by:

$$\frac{d}{dt} y_{ijk}^{(1,L/R)} = -y_{ijk}^{(1,L/R)} + (1 - y_{ijk}^{(1,L/R)})(S_{ijk}^{L/R} + \eta x_{ijk}^{(1,L/R)}) - (y_{ijk}^{(1,L/R)} + 1) \sum_{pq \in N_{ij}} W_{pqijk} m_{pq}^{L/R}, \tag{9}$$

where η=3. The LGN and layer 6 activate layer 4 through terms $S_{ijk}^{L/R}$ and $\eta x_{ijk}^{(1,L/R)}$, respectively. The activity of inhibitory interneurons $m_{pq}^{L/R}$ connecting layer 6 to layer 4 of V1 is passed through an elongated Gaussian kernel W_{pqijk}:

$$W_{pqijk} = \frac{1}{2\pi(\sigma_1^2 + \sigma_2^2)} \exp\left(-\frac{1}{2} \left(\frac{(p-i)^2}{\sigma_1^2} + \frac{(q-j)^2}{\sigma_2^2} \right) \right). \tag{10}$$

For the vertical orientation (*k* = 1, 3), σ_1 = 10 and σ_2 =1, which defines a vertical elongated receptive field. For the horizontal orientation (*k* = 2, 4), σ_1 = 1 and σ_2 =10, and the interlayer connection is elongated horizontally. The shape of the kernel W_{pqijk} for the vertical orientation (*k*=1, 3) is shown in Figure A1a.

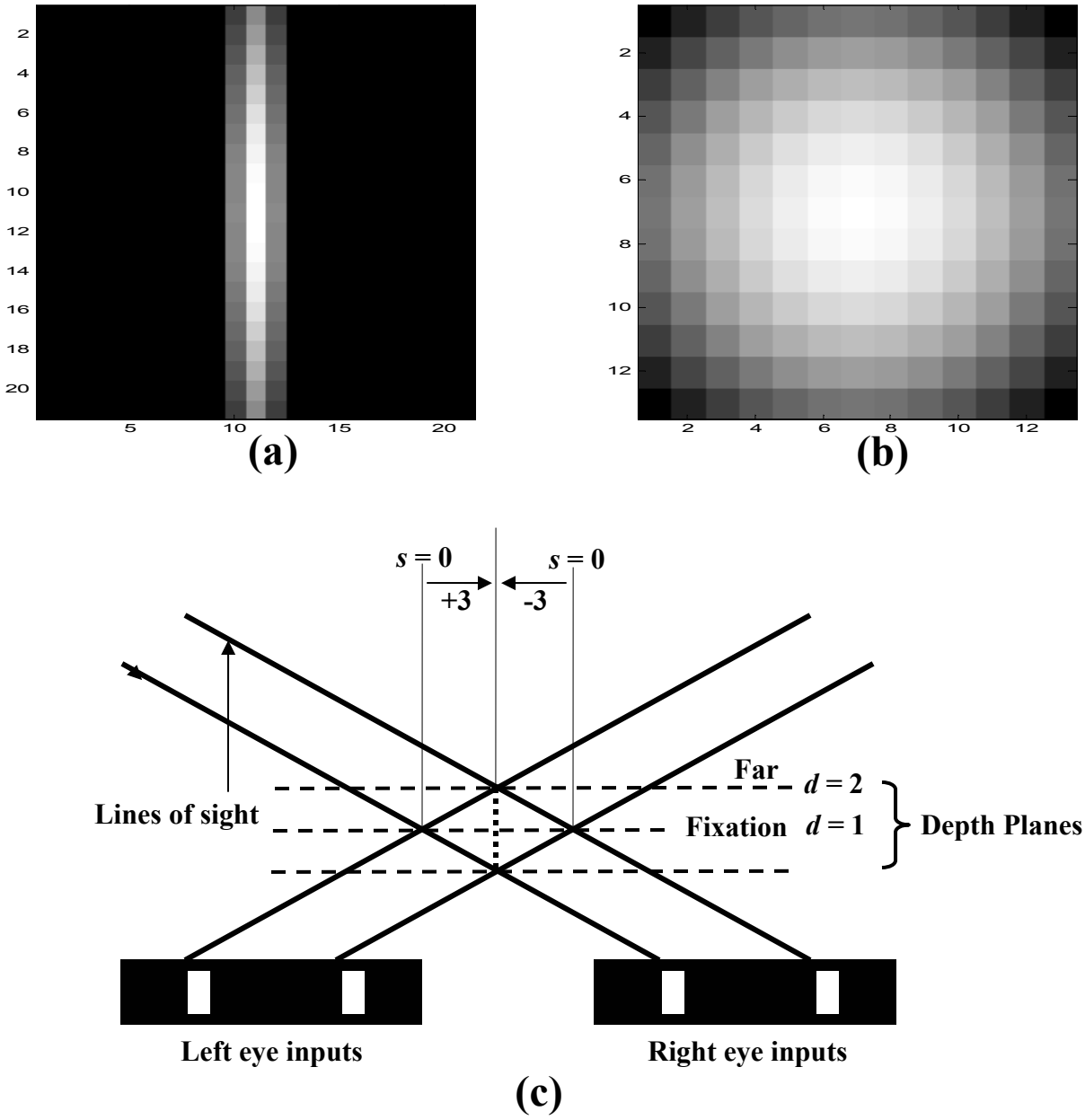

Figure A1. **(a) Depiction of the vertical inhibitory kernel of W for equation (5). (b) Depiction of orientation competition kernel in equation (11). (c) Line of sight, allelotropic shifts, and demonstration of different depth planes.**

Equation (9) implements the like-polarity competition between the layer 4 simple cells of V1, because the same index k on both sides of (9) restricts the competition to the same orientation and polarity. At equilibrium, (9) becomes:

$$y_{ijk}^{(1+L/R)} = \frac{S_{ijk}^{(L/R)} + \eta x_{ijk}^{(1,L/R)} - \sum_{pq \in N_{ij}} W_{pqijk} m_{pq}^{(L/R)}}{1 + S_{ijk}^{(L/R)} + \eta x_{ijk}^{(1,L/R)} + \sum_{pq \in N_{ij}} W_{pqijk} m_{pq}^{(L/R)}}. \tag{11}$$

The inhibitory interneuron activity $m_{ijk}^{L/R}$ follows the equation:

$$\frac{d}{dt}m_{ijk}^{L/R} = -m_{ijk}^{L/R} + \eta^{-}x_{ijk}^{(1,L/R)} - m_{ijk}^{L/R}\sum_{pq\in N_{ij}} W_{pqijk}^{-} m_{pq}^{L/R}. \tag{12}$$

Kernel W_{pqijk}^{-} is a linearly scaled version of W_{pqijk} in (10); namely, $W_{pqijk}^{-} = 0.15\,W_{pqijk}$. Equation (12) implements the property that inhibitory interneurons inhibit each other to normalize the total inhibition. The importance of this property was described in Grossberg and Raizada (2000).

A4. V1 layer 3B: Vertical binocular simple cells

The vertically oriented layer 3B cells with activity $b_{ijkd}^{(1,B)}$ (k=1 or 3) binocularly fuse inputs from layer 4 vertically oriented monocular simple cells that are sensitive to the same polarity of contrast. In equilibrium, $b_{ijkd}^{(1,B)}$ is determined by:

$$b_{ijkd}^{(1,B)} = \frac{1}{\gamma_1}\left([y_{(i-s)jk}^{(1,R)}]^{+} + [y_{(i+s)jk}^{(1,L)}]^{+} - \alpha\left([q_{ijkd}^{L}]^{+} + [q_{ijrd}^{L}]^{+} + [q_{ijkd}^{R}]^{+} + [q_{ijrd}^{R}]^{+}\right)\right), \tag{13}$$

where α =5 and γ_1 = 8.5. The obligate simple cell $b_{ijkd}^{(1,B)}$ is excited by layer 4 simple cells of both ocularities with the same polarity (index k in $y_{(i-s)jk}^{(1,R)}]^{+} + [y_{(i+s)jk}^{(1,L)}]^{+}$). Index d shows the depth plane, d = 1 for the near depth and d =2 for the far depth. The parameters $i+s$ and $i-s$ indicate the shifted monocular positions corresponding to the binocular positions i in each depth plane. As can be seen in Figure A1c, the retinal images of both eyes can be projected back along the line of sight onto the fixation plane (d = 1, Figure A1c). There, these retinal images match correspondingly. Following the retinal images along the lines of sight onto the far depth plane is associated with horizontal displacement of corresponding retinal images. This horizontal shift, compared to the corresponding position on the fixation plane and dependent on the depth plane and the eye of origin, is called an allelotropic shift and its amount is shown by index s. For d = 1 (near depth, fixation plane in Figure A1c), s =0. For the far depth (d = 2), s = 3. The direction of allelotropic shift is opposite for opposite ocularities. Therefore the horizontal coordinates of left and right monocular excitatory inputs from layer 4 to 3B is shifted oppositely (+s and –s in $[y_{(i+s)jk}^{(1,L)}]^{+}$ and $[y_{(i-s)jk}^{(1,R)}]^{+}$ on the right hand side of (13)).

The obligate simple cell activity $b_{ijkd}^{(1,B)}$ is inhibited by all like-oriented inhibitory interneurons at their position (i,j), including those with opposite polarities (indices k and r) via terms $[q_{ijkd}^{L}]^{+} + [q_{ijrd}^{L}]^{+}$ and $[q_{ijkd}^{R}]^{+} + [q_{ijrd}^{R}]^{+}$ in (13). These eye-specific inhibitory cells at layer 3B with activities $q_{ijkd}^{L/R}$ respond to the vertical orientation (k=1 and 3):

$$\frac{dq_{ijkd}^{L}}{dt} = -\gamma_2 q_{ijkd}^{L} + [y_{(i+s)jk}^{(1,L)}]^{+} - \beta\left([q_{ijkd}^{R}]^{+} + [q_{ijrd}^{R}]^{+} + [q_{ijrd}^{L}]^{+}\right) \tag{14}$$

and

$$\frac{dq_{ijkd}^{R}}{dt} = -\gamma_2 q_{ijkd}^{R} + [y_{(i-s)jk}^{(1,R)}]^{+} - \beta\left([q_{ijkd}^{L}]^{+} + [q_{ijrd}^{L}]^{+} + [q_{ijrd}^{R}]^{+}\right), \tag{15}$$

where γ_2 and β are constants (1 and 5, respectively), and $r = 4 - k$ to provide the opposite-polarity orientation index. As shown in Figure 7, these layer 3B inhibitory cells get excited by layer 4 cells (terms $[y_{(i+s)jk}^{(1,L)}]^{+}$ and $[y_{(i-s)jk}^{(1,R)}]^{+}$ on the right hand sides of (14) and (15), respectively) and inhibition from inhibitory interneurons of opposite ocularity with both polarities (reflected by k and r in terms $[q_{ijkd}^{R}]^{+} + [q_{ijrd}^{R}]^{+}$ and $[q_{ijkd}^{L}]^{+} + [q_{ijrd}^{L}]^{+}$ on the right hand side of (14) and (15), respectively), as well as inhibition from the inhibitory interneuron with opposite polarity with the same ocularity (terms $[q_{ijrd}^{L}]^{+}$ and $[q_{ijrd}^{R}]^{+}$ on the right hand side of (14) and (15), respectively).

In (13), the same-polarity inhibition (indicated by index k) assures that these binocular simple cells obey an *obligate property* (Poggio, 1991); that is, they can be activated only when they get

excitatory input $[y^{(1,R)}_{(i-s)jk}]^+ + [y^{(1,L)}_{(i+s)jk}]^+$ from both ocularities of layer 4 simple cells. The opposite polarity inhibition (indicated by index *r*) assures that obligate cells do not fuse edges with opposite polarities. A mathematical proof of these properties is described in Grossberg and Howe (2003).

An additional property of the present simulations with regard to the obligate cells is the *size-disparity correlation* (Kulikowski, 1978; Richards and Kaye, 1974; Schor and Tyler, 1981; Schor and Wood, 1983; Schor, Wood, and Ogawa, 1984; Tyler, 1975, 1983). FACADE theory (Grossberg, 1994) exploits the fact that binocularly driven cells with larger receptive fields have a broader range of binocular fusion and can tolerate larger disparity value offsets from their optimum value. This phenomenon implies that many binocular cells can signal the presence of vertical boundaries in more than one depth plane. In the present simulations, we consider two depth planes for simplicity (see Grossberg and Howe (2003) for simulations with more than two depth planes). Obligate cells in both depth planes can hereby signal the vertical edges of 2D images. Obligate cells at both depth planes are assumed to experience a small *s* (=3) difference in (13) which does not exceed the effective width of their receptive field kernels. This is why, initially and before monocular FIDO feedback, the *vertical* boundaries are present at both depths; see, for example, Figures 11a and 15a.

A5. V1 layer 3B: Monocular simple cells

Figure 7 shows that, besides the vertical binocular simple cells, there are monocular simple cells with activity $b^{(1,L/R)}_{ijk}$ that are driven by monocular simple cells in layer 4 of V1:

$$b^{(1,L/R)}_{ijk} = [y^{(1,L/R)}_{ijk}]^+. \tag{16}$$

A6. V1 layer 2/3: Complex cells

Complex cells of layer 2/3 with activity $z^{(1,L/R/B)}_{ijkd}$ pool opposite polarity input from layer 3B cells. Within a spatial region, complex cells that are tuned to perpendicular orientations also compete. As in layer 3B, layer 2/3 contains both monocular and binocular complex cells, which have their own opposite-polarity pooling and orientational competition independent from each other. The stimulus of Figure 3 and 4 illustrate the importance of such separation, because all contrastive edges there are monocular. Layer 2/3 complex cell activities $z^{(1,L/R/B)}_{ijrd}$ obey:

$$\begin{aligned}\frac{d}{dt} z^{(1,L/R/B)}_{ijkd} = &-z^{(1,L/R/B)}_{ijkd} + (1 - z^{(1,L/R/B)}_{ijkd})([b^{(1,L/R/B)}_{ijkd}]^+ + [b^{(1,L/R/B)}_{ijrd}]^+) - \\ &(1 + z^{(1,L/R/B)}_{ijkd}) \sum_{pq} N_{pqij} ([b^{(1,L/R/B)}_{pqKd}]^+ + [b^{(1,L/R/B)}_{pqRd}]^+).\end{aligned} \tag{17}$$

In (17), because complex cells pool over opposite polarities, *k* = 1, 2 (vertical, horizontal). Term $[b^{(1,L/R/B)}_{ijkd}]^+ + [b^{(1,L/R/B)}_{ijrd}]^+$ describes pooling of the like-oriented but opposite-polarity layer 3B inputs with orientation indices *k* and *r*, respectively. Indices *K* and *R* denote the orientations perpendicular to *r* and *k*, respectively with opposite polarity. Term $\sum_{pq} N_{pqij} ([b^{(1,L/R/B)}_{pqKd}]^+ + [b^{(1,L/R/B)}_{pqRd}]^+)$ describes inhibitions from perpendicular orientations (with opposite polarities) within a neighborhood of (*i,j*) with Gaussian kernel:

$$N_{pqij} = \frac{1}{2\pi\sigma^2} \exp\left(-\frac{1}{2\sigma^2} ((p-i)^2 + (q-j)^2) \right), \tag{18}$$

where $\sigma = 3$ (Figure A1b).

A7. V2 layer 4

Monocular and binocular V1 layer 2/3 cell outputs $z_{ijk}^{(1,L/R)}$ and $z_{ijkd}^{(1,B)}$, respectively, are pooled in layer 4. This hypothesis is consistent with the fact that most cells in V2 are binocular (Hubel and Livingstone, 1987). The activity $y_{ijkd}^{(2)}$ of a V2 layer 4 horizontal cell ($k = 2$) pools monocular V1 outputs:

$$\frac{d}{dt} y_{ijkd}^{(2)} = -y_{ijkd}^{(2)} + \left[z_{(i+s)jk}^{(1,L)}\right]^+ + \left[z_{(i-s)jk}^{(1,R)}\right]^+ - \delta \sum_{e<d} F(p_{ije}^L + p_{ije}^R). \tag{19}$$

The vertical orientation ($k = 1$) V2 layer 4 cell pools both monocular and binocular V1 outputs:

$$\frac{d}{dt} y_{ijkd}^{(2)} = -y_{ijkd}^{(2)} + \left[z_{ijkd}^{(1,B)}\right]^+ + \upsilon\left(\left[z_{(i+s)jk}^{(1,L)}\right]^+ + \left[z_{(i-s)jk}^{(1,R)}\right]^+\right) - \delta \sum_{e<d} (p_{ije}^L + p_{ije}^R). \tag{20}$$

In (19) and (20), parameters $\upsilon = 0.20$ and $\delta = 10$. The pruning signal $p_{ije}^{L/R}$ of the monocular FIDO (Figure 8, from equation (38)) inhibits $y_{ijkd}^{(2)}$ when the latter is at a farther depth ($e < d$: larger index represent farther depth).

A8. V2 layer 2/3: Bipole grouping cells

The bipole property is realized by interactions between long-range cooperation and short-range competition, as shown in Figure 7. Variable $z_{ijkd}^{(2)}$ represents the bipole cell activity at layer 2/3 of V2:

$$\frac{d}{dt} z_{ijkd}^{(2)} = -z_{ijkd}^{(2)} + (1 - z_{ijkd}^{(2)})([y_{ijkd}^{(2)}]^+ + Q_{ijkd}^{(1)} + Q_{ijkd}^{(2)}) - (z_{ijkd}^{(2)} + \psi)(Q_{ijkd}^{Is} + Q_{ijkd}^{Io} + Q_{ijkd}^{Id}). \tag{21}$$

The excitatory bottom-up input $[y_{ijkd}^{(2)}]^+$ from layer 4 sums with $Q_{ijkd}^{(1)}$ and $Q_{ijkd}^{(2)}$ which are obtained by convolving elongated half-Gaussian kernels $H_{pqijk}^{(v)}$ with layer 2/3 bipole cell outputs (Figure 7):

$$Q_{ijkd}^{(v)} = \sum_{pq} H_{pqijk}^{(v)} [z_{ijkd}^{(2)} - \rho_z]^+, \tag{22}$$

$v = 1, 2$. Kernels $H_{pqijk}^{(1)}$ and $H_{pqijk}^{(2)}$ in (22) are derived from the Gaussian kernel H_{pqijk}:

$$H_{pqijk} = \frac{1}{2\pi(\sigma_1^2 + \sigma_2^2)} \exp\left(-\frac{1}{2}\left(\frac{(p-i)^2}{\sigma_1^2} + \frac{(q-j)^2}{\sigma_2^2}\right)\right). \tag{23}$$

The horizontally oriented half-Gaussian $H_{pqijk}^{(1)}$ is determined by setting $k = 2$, σ_1 =8, σ_2 =1, and H_{pqijk} to zero when $p < i$. Setting H_{pqijk} to zero when $p > i$ results in $H_{pqijk}^{(2)}$. The vertically oriented half-Gaussian $H_{pqijk}^{(1)}$ is determined by setting $k = 1, \sigma_1 = 1$, σ_2 =8, and H_{pqijk} to zero when $q < j$. Likewise, $q < j$ results in $H_{pqijk}^{(2)}$.

As Figure 7 shows, inhibitory interneurons with activity s_{ijkdv} from both sides ($v = 1, 2$) inhibit bipole cells in order to realize the selective inward propagation of boundary completion. Correspondingly, the inhibitory terms, Q_{ijkd}^{Is}, in (21) pool the activity of inhibitory interneurons s_{ijkdv} from both sides at each position:

$$Q_{ijkd}^{Is} = \sum_{v=1,2} [s_{ijkdv}]^+. \tag{24}$$

Inhibitory interneurons with activities s_{ijkdv} get their excitatory input from horizontal connections on the same side of the bipole cell and their inhibitory inputs from the opposite side ($u \neq v$) and the same position (i,j):

$$\frac{d}{dt} s_{ijkdv} = -s_{ijkdv} + Q_{ijkd}^{(v)} - \mu_s s_{ijkdv} [s_{ijkdu}]^+. \tag{25}$$

Each bipole cell is also inhibited by orientational competition from the bipole cells of the perpendicular orientation ($r \neq k$) within a spatial region around each position (i,j), as implemented by term Q_{ijkd}^{Io} in (21):

$$Q_{ijkd}^{Io} = \sum_{pq}^{r \neq k} N_{pqij} [z_{pqrd}^{(2)} - \rho_z]^+, \tag{26}$$

where N_{pqij} is the same kernel as in (17).

Vertically oriented bipole cells with activities $z_{ijkd}^{(2)}$ (k = 1) are also influenced by a *disparity filter* that inhibits false binocular matches. Each vertically oriented bipole cell is inhibited by every other vertically oriented bipole cell that shares one of its monocular inputs (Figure A1c, oblique line of sight), or is directly in front of or behind it (Figure A1c, dashed vertical line): The term Q_{ijkd}^{Id} in (23) provides such inhibition:

$$Q_{ijkd}^{Id} = \omega_1 \sum_{d' \neq d} \left(m_{dd'} \left[z_{(i+s'-s)jkd'}^{(2)} \right]^+ + m_{dd'} \left[z_{(i+s-s')jkd'}^{(2)} \right]^+ + \omega_2 \left[z_{ijkd'}^{(2)} \right]^+ \right). \tag{27}$$

Parameter $m_{dd'}$ = 1.3 when d = 1 (near) and d' = 2 (far). Parameter $m_{dd'}$ = 2.8 when d = 2 (far) and d' = 1 (near). The near plane (fixation plane) is preferred because inhibition from near-to-far is larger than inhibition from far-to-near. As a result, the monocular boundary activities corresponding to the stimulus of Figure 3 will be assigned to zero depth. For the horizontal orientation (k = 2), Q_{ijkd}^{Id} = 0. In the other words, the disparity filter acts on the vertical orientation. Parameters in (21) - (27) are ψ = 0.9, ρ_z = 0.05 and μ_s = 12 ω_1 = 0.4 and ω_2 = 0.1.

The disparity filter in the 3D LAMINART model of Grossberg and Howe (2003) used a recurrent network equation similar to (27). That model did not, however, include perceptual grouping using bipole cells. Cao and Grossberg (2004) augmented the Grossberg and Howe (2003) model to include bipole-based perceptual grouping, as in the articles of Grossberg and Raizada (2000) and Grossberg and Swaminathan (2004). In addition, Cao and Grossberg (2004), showed how the disparity filter could suppress groupings that correspond to false matches by using an equation like (27). This augmented model was used to explain data about stereopsis and 3D planar surface perception that Grossberg and Howe (2003) could not. The present article shows how this equation can also form part of an explanation of 3D stratification, transparency, and 3D neon color spreading.

A9. Surface representation and monocular FIDO

The BCS boundary signals that block filling-in are defined by the sum across all orientations of bipole cell outputs at each position and depth:

$$Z_{ijd} = \sum_{k=1}^{2} z_{ijkd}^{(2)}. \tag{28}$$

Filling-in dynamics are governed by a boundary-gated diffusion equation in which $F_{ijd}^{L/R,+}$ is the monocular Left/Right ON surface signal at position (i, j) and depth d:

$$\frac{d}{dt} F_{ijd}^{L/R+} = -mF_{ijd}^{L/R+} + \sum_{(p,q) \in N_{ij}} (F_{pqd}^{L/R+} - F_{ijd}^{L/R+}) P_{pqijd}^{(M)} + X_{(i \pm s)j}^{L/R+}. \tag{29}$$

The diffusion coefficients, $P_{pqijd}^{(M)}$, in the monocular FIDO are defined by:

$$P_{pqijd}^{(M)} = \frac{\delta}{1 + \varepsilon (Z_{pqd} + Z_{ijd})}, \tag{30}$$

where ε = 1,000,000, δ = 10, and for d =1 and 2, s = 0 and 3, respectively.

LGN inputs are shifted along the line of sight to match their corresponding boundaries at each depth, as reflected by indices $i \pm s$ within $X_{(i \pm s)j}^{L/R+}$ in (32); see Grossberg, Hwang and Mingolla (2002) for how this may happen through learning. At equilibrium, (32) becomes:

$$F_{ijd}^{L/R+} = \frac{X_{(i\pm s)j}^{L/R+} + \sum_{(p,q)\in N_{ij}} F_{pqd}^{L/R+} P_{pqijd}^{M}}{m + \sum_{(p,q)\in N_{ij}} P_{pqijd}^{M}}, \tag{31}$$

where $m = 1$, and the diffusion occurs between nearest neighbors $N_{ij} = \{(i, j-1), (i-1, j), (i+1, j), (i, j+1)\}$. Equation (34) is solved by giving zero initial values to $F_{pqd}^{L/R+}$ and iteratively passing the resultant values of $F_{ijd}^{L/R+}$ to the left hand side of (34) until the recursion equilibrates.

The same dynamics govern OFF filling-in with $F_{ijd}^{L/R-}$ representing the filled-in OFF surface activity:

$$\frac{d}{dt} F_{ijd}^{L/R-} = -mF_{ijd}^{L/R-} + \sum_{(p,q)\in N_{ij}} (F_{pqd}^{L/R-} - F_{ijd}^{L/R-}) P_{pqijd}^{M} + X_{(i\pm s)j}^{L/R-}. \tag{32}$$

At equilibrium, (35) becomes:

$$F_{ijd}^{L/R-} = \frac{X_{(i\pm s)j}^{L/R-} + \sum_{(p,q)\in N_{ij}} F_{pqd}^{L/R-} P_{pqijd}^{M}}{m + \sum_{(p,q)\in N_{ij}} P_{pqijd}^{M}}. \tag{33}$$

The monocular FIDO output is defined by:

$$R_{ijd}^{L/R} = \left[F_{ijd}^{L/R+} - F_{ijd}^{L/R-}\right]^{+}. \tag{34}$$

This double-opponent filled-in signal can cancel when there is a gap in the boundary signal of an edge: The ON filling-in spreads across the gap from one side of it, whereas the OFF filling-in spread across the gap from the other side. Because the ON filling-in activity then equals the OFF filling-in activity on both sides of the boundary gap, they cancel each other in (37). Therefore, any surface whose boundary has a big gap cannot fill-in efficiently unless another connected boundary surrounds it at sufficiently close proximity.

A10. Monocular FIDO output

To generate boundary pruning signals b_{ijd} from the near depth to the far depth in (20) (see Figure 11b), filled-in activities at the Monocular FIDOs are passed through a contrast-sensitive on-center off-surround kernel:

$$\frac{d}{dt} p_{ijd}^{L/R} = -\alpha_b p_{ijd}^{L/R} + (U_b - p_{ijd}^{L/R}) C_{bd}^{L/R} - (L_b + p_{ijd}^{L/R}) E_{bd}^{L/R}. \tag{35}$$

The on-center term

$$C_{bd}^{L/R} = \sum_{(p,q)\in N_{ij}} C_{pq} R_{i+p,j+q,d}^{L/R} \tag{36}$$

has a Gaussian kernel:

$$C_{pq} = \frac{C}{2\pi\sigma_c^2} \exp\left(-\frac{p^2+q^2}{2\sigma_c^2}\right), \tag{37}$$

as does the off-surround term:

$$E_{bd}^{L/R} = \sum_{(p,q)\in N_{ij}} E_{pq} R_{i+p,j+q,d}^{L/R}, \tag{38}$$

where

$$E_{pq} = \frac{S}{2\pi\sigma_s^2} \exp\left(-\frac{p^2+q^2}{2\sigma_s^2}\right). \tag{39}$$

Parameters in (38)-(42) are α_b=1, U_b=1, L_b=1, C=1, $\sigma_c = 3$, S=0.75, $\sigma_s = 3$.

A11. Pruned surface signals within the Binocular FIDO

Visible surface signals occur at the binocular FIDOs. Here, binocularly matched LGN signals from both eyes activate depth-selective filling-in domains (pathway 8 in Figure 8), while the contrast-sensitive Monocular FIDO outputs of nearer depths from both eyes prune, or inhibit, redundant surface signals at the same positions and further depths (pathways 9 in Figure 8). The activity ϕ_{ijd} of a Binocular FIDO cell at position (*i,j*) and depth *d* thus obeys:

$$\frac{d}{dt}\phi_{ijd}^{+/-} = -\alpha_{bf}\phi_{ijd}^{+/-} + (U_{bf} - \phi_{ijd}^{+/-})(X_{(i+s)j}^{L+/-} + X_{(i-s)j}^{R+/-}) - (L_{bf} + \phi_{ijd}^{+/-})\sum_{e<d}(p_{ije}^{L} + p_{ije}^{R}), \quad (40)$$

where the LGN inputs are defined by (28) and (30) and the pruning signal by (38). For d = 1 (near), s = 0, and for d = 2 (far), s =3. Parameters U_{bf} and L_{bf} equal 1.

Because there are only two depth planes, the above equation is just applicable when d = 2 and e = 1, equivalent to the pruning of the far depth by the near depth (larger depth index means farther).

A12. Binocular FIDO surface formation using enriched boundaries

Finally, activities $\mu_{ijd}^{+/-}$ represent the ON and OFF filled-in surface representation at the Binocular FIDOs:

$$\frac{d}{dt}\mu_{ijd}^{+/-} = -m\mu_{ijd}^{+/-} + \sum_{(p,q)\in N_{ij}}(\mu_{pqd}^{+/-} - \mu_{ijd}^{+/-})P_{pqijd}^{B} + \phi_{ijd}^{+/-}. \quad (41)$$

In (44), terms P_{pqijd}^{B} represent the boundary-gated permeabilities:

$$P_{pqijd}^{B} = \frac{\delta}{1 + \varepsilon(\xi_{pqd} + \xi_{ijd})}. \quad (42)$$

At the binocular FIDOs, the boundaries that determine gating are enriched (e.g., Figure 15c and 18b) by adding all nearer boundaries at each position:

$$\xi_{ijd} = \sum_{e\le d} Z_{ije}. \quad (43)$$

The same method used to solve (34) is used for (44). The double-opponent filled-in activity, $R_{ijd}^{(B)}$, represents the visible surface percept:

$$R_{ijd}^{(B)} = \left[\mu_{ijd}^{+} - \mu_{ijd}^{-}\right]^{+}. \quad (44)$$

References

Adelson, EH. (2000). Lightness Perception and Lightness Illusions. In: M. Gazzaniga (Ed.), *The New Cognitive Neurosciences* (pp. 339-351). 2nd Ed. Cambridge, MA: MIT Press.

Anderson, BL. (1997). A theory of illusory lightness and transparency in monocular and binocular images: the role of contour junctions. *Perception*, *26*:419-53

Backus, BT., Fleet, DJ., Parker, AJ., & Heeger, DJ. (2001). Human cortical activity correlates with stereoscopic depth perception. *Journal of Neurophysiology, 86,* 2054-2068

Beck J, Prazdny K, & Ivry R. (1984). The perception of transparency with achromatic colors, *Perception and Psychophysics, 35*: 407-22

Cao, Y., & Grossberg S. (2004). A laminar cortical model of stereopsis and 3D surface perception: Closure and da Vinci stereopsis. *Spatial Vision*, in press

DeWeerd, P., Peralta, MR., Desimone, R., & Ungerledier, LG. (1999). Loss of attentional stimulus selection after extrastriate cortical lesions in macaques. *Nature Neuroscience*, *2*, 753-758

Dresp B & Grossberg S. (1997). Contour integration across polarities and spatial gaps: from local contrast filtering to global grouping, *Vision Research 37*:913-24

Dresp B & Grossberg S. (1999). Spatial facilitation by color and luminance edges: boundary, surface, and attentional factors, *Vision Research 39*:3431-43

Dresp B, Durand S, & Grossberg S. (2002). Depth perception from pairs of overlapping cues in pictorial displays. *Spatial Vision 15*: 255-76

Grossberg S. (1980). How does a brain build a cognitive code? *Psychological Review, 87*:1-51

Grossberg S. (1994). 3-D vision and Figure-ground separation by visual cortex. *Perception and Psychophysics*, *55*: 48-121

Grossberg S. (1997). Cortical dynamics of three-dimensional Figure-ground perception of two-dimensional pictures, *Psychological Review, 104*:618-58

Grossberg S. (1999a). How does the cerebral cortex work? Learning, attention, and grouping by the laminar circuits of visual cortex. *Spatial Vision, 12*:163-85

Grossberg S. (1999b). The link between brain learning, attention, and consciousness. *Consciousness and Cognition*, *8*:1-44

Grossberg S. (2003). Filling-in the forms: Surface and boundary interactions in visual cortex. In L. Pessoa, & P. DeWeerd (Eds.), *Filling-In: From Perceptual Completion to Cortical Reorganization* (pp.13-37). New York: Oxford University Press.

Grossberg, S., & Howe, P.D.L. (2003). A laminar cortical model of stereopsis and three-dimensional surface perception. *Vision Research*, *43*:801-29

Grossberg S, Hwang S, Mingolla E. (2002). Thalamocortical dynamics of the McCollough effect: boundary-surface alignment through perceptual learning. *Vision Research*, *42*:1259-86

Grossberg S. & Kelly F. (1999). Neural dynamics of binocular brightness perception, *Vision Research, 39*: 3796-816

Grossberg S, & Mingolla E. (1985a). Neural dynamics of perceptual grouping: textures, boundaries, and emergent segmentations. *Perception and Psychophysics*, *38*:141-71

Grossberg S, & Mingolla E. (1985b). Neural dynamics of form perception: boundary completion, illusory figures, and neon color spreading. *Psychological Review*, *92*:173-211

Grossberg S, Mingolla E, & Ross WD. (1997). Visual brain and visual perception: how does the cortex do perceptual grouping? *Trends in Neurosciences*, *20*:106-11

Grossberg S, & Raizada RD. (2000). Contrast-sensitive perceptual grouping and object-based attention in the laminar circuits of primary visual cortex, *Vision Research*, *40*:1413-32

Grossberg S, & Seitz A. (2003). Laminar development of receptive fields, maps and columns in visual cortex: the coordinating role of the subplate, *Cerebral Cortex*, *13*:852-63

Grossberg S. & Swaminathan G. (2003). A laminar cortical model for 3D perception of slanted and curved surfaces and of 2D images: Development, attention, and bistability Technical Report CAS/CNS TR-2003-002, Boston University. Submitted for publication

Grossberg S, & Todorovic D. (1988). Neural dynamics of 1-D and 2-D brightness perception: a unified model of classical and recent phenomena, *Perception and Psychophysics*, *43*: 241-77

Grossberg S, Williamson JR. (2001). A neural model of how horizontal and interlaminar connections of visual cortex develop into adult circuits that carry out perceptual grouping and learning, *Cerebral Cortex, 11*: 37-58

Grossberg S., & Yazdanbakhsh A. (2003a). Laminar cortical dynamics of 3D surface stratification, transparency, and neon spreading. *3rd annual meeting of Vision Sciences Society*, *FR43,* pp. 77

Grossberg S., & Yazdanbakhsh A. (2003b). Laminar Cortical Mechanisms of 3D Surface Processing, *Society for Neuroscience 33rd annual meeting*, 339.5

Howe PD. (2000). A comment on the Anderson (1997), the Todorovic (1997), and the Ross and Pessoa (2000) explanations of White's effect. *Perception, 30*: 1023-6

Howe PD. & Watanabe T. (2003). Measuring the depth induced by an opposite-luminance (but not anticorrelated) stereogram, *Perception, 32*: 415-21

Hubel, DH., & Livingstone, MS. (1987). Segregation of form, color, and stereopsis in primate area 18. *The Journal of Neuroscience*, *7,* 3378-3415.

Hubel DH, & Wiesel TN. (1968). Receptive fields and functional architecture of monkey striate cortex, *Journal of Physiology*, *195*:215-43

Kelly F, & Grossberg S. (2000). Neural dynamics of 3-D surface perception: Figure-ground separation and lightness perception, *Perception and Psychophysics*, *62*:1596-618

Kulikowski JJ. (1978). Limit of single vision in stereopsis depends on contour sharpness, *Nature. 275*: 126-7

Metelli F. (1974). The perception of transparency, *Scientific American*, *230*:90-8

McGuire BA, Hornung JP, Gilbert CD, & Wiesel TN. (1984). Patterns of synaptic input to layer 4 of cat striate cortex. *Journal of Neuroscience*, *4*:3021-33

Nakamura, K., & Colby, C. L. (2000a). Visual, saccade-related, and cognitive activation of single neurons in monkey extrastriate area V3A. *Journal of Neurophysiology, 84,* 677-692.

Nakamura, K., & Colby, C. L. (2000b). Updating of the visual representation in monkey striate and extrastriate cortex during saccades. *Proceedings of the National Academy of Sciences, 99,* 4026-4031

Nakamura, H., Kuroda, T., Wakita, M., Kusunoki, M., Kato, A., Mikami, A., Sakata, H., & Itoh, K. (2001). From three-dimensional space vision to prehensile hand movements: The lateral intraparietal area links the area V3A and the anterior intraparietal area in macaque. *The Journal of Neuroscience*, *21*, 8174-8187

Nakayama K. (1996). Binocular visual surface perception *Proceedings of the National Academy of Sciences U S A*, *23;93*:634-9

Poggio, GF. (1991). Physiological basis of stereoscopic vision. In *Vision and Visual Dysfunction. Binocular vision* (pp. 224-238). Boston, MA: CRC

Polat U, & Sagi D. (1993). Lateral interactions between spatial channels: suppression and facilitation revealed by lateral masking experiments, *Vision Research*, 33(7):993-9

Raizada RD, & Grossberg S. (2003). Towards a theory of the laminar architecture of cerebral cortex: computational clues from the visual system, *Cerebral Cortex*, *13*:100-13

Richards W, & Kaye MG. (1974). Local versus global stereopsis: two mechanisms? *Vision Research.14*: 1345-7

Schor CM, & Tyler CW. (1981). Spatio-temporal properties of Panum's fusional area, *Vision Research, 21*: 683-92

Schor CM, & Wood I. (1983). Disparity range for local stereopsis as a function of luminance spatial frequency, *Vision Research, 23*: 1649-54

Schor C, Wood I, & Ogawa J. (1984). Binocular sensory fusion is limited by spatial resolution. *Vision Research, 24*:661-5

Takeichi H, Shimojo S, & Watanabe T. (1992). Neon flank and illusory contour: interaction between the two processes leads to color filling-in. *Perception*, *21*:313-24

Tootell, RBH., Mendola, JD., Hadjikhani, NK., Ledden, PJ., Liu, AK., Reppas, JB., Sereno, M. I., & Dale, A. M. (1997). Functional analysis of V3A and related areas in human visual cortex. *The Journal of Neuroscience*, *17,* 7060-7078

Tsao DY, Vanduffel W, Sasaki Y, Fize D, Knutsen TA, Mandeville JB, Wald LL, Dale AM, Rosen BR, Van Essen DC, Livingstone MS, Orban GA, & Tootell RB. (2003). Stereopsis activates V3A and caudal intraparietal areas in macaques and humans, *Neuron, 39*: 555-68

Tucker TR, & Katz LC. (2003a). Recruitment of local inhibitory networks by horizontal connections in layer 2/3 of ferret visual cortex. *Journal of Neurophysiology, 89*:501-12
Tucker TR, Katz LC. (2003b). Spatiotemporal patterns of excitation and inhibition evoked by the horizontal network in layer 2/3 of ferret visual cortex. *Journal of Neurophysiology*, *89*:488-500

Tyler CW. (1975). Spatial organization of binocular disparity sensitivity, *Vision Research, 15*: 583-90

Tyler CW. (1983). Sensory processing of binocular disparity. In C. M. Schor & K. J. Cuiffreda (Eds.), *Vergence eye movements* (pp. 199-295). Boston: Butterworths

von der Heydt R, Peterhans E, Baumgartner G. (1984). Illusory contours and cortical neuron responses, *Science*, *224*:1260-2

Watanabe T, Cavanagh P. (1993). Surface decomposition accompanying the perception of transparency, *Spatial Vision,* 7:95-111

Watanabe T, Cavanagh P. (1993). Transparent surfaces defined by implicit X junctions, *Vision Research*, *33*:2339-46

Yazdanbakhsh A, Watanabe T. (2004). Asymmetry between horizontal and vertical illusory lines in determining the depth of their embedded surface, *Vision Research 44*: 2621-7